Title

Evolutionarily divergent mTOR remodels translatome for tissue regeneration.

Permalink

Journal

Authors

Zhulyn, Olena
Rosenblatt, Hannah
Shokat, Leila
et al.

Publication Date

DOI

Peer reviewed

Evolutionarily divergent mTOR remodels translatome for tissue regeneration

Olena Zhulyn[1,2,3], **Hannah D. Rosenblatt**[1,2], **Leila Shokat**[1], **Shizhong Dai**[4], **Duygu Kuzuoglu-Öztürk**[5,6], **Zijian Zhang**[1,7], **Davide Ruggero**[4,5,6], **Kevan M. Shokat**[4,8], **Maria Barna**[1,9]

[1]Department of Genetics, Stanford University School of Medicine, Stanford, CA 94305, USA

[2]Department of Developmental Biology, Stanford University, Stanford, CA 94305, USA

[3]Current address: Department of Developmental & Stem Cell Biology, SickKids Research Institute, Toronto, ON, Canada

[4]Department of Cellular and Molecular Pharmacology, University of California, San Francisco, CA 94158, USA

[5]Department of Urology, University of California, San Francisco, San Francisco, CA, USA

[6]Helen Diller Family Comprehensive Cancer Center, University of California, San Francisco, San Francisco, CA 94158, USA

[7]Department of Chemical and Systems Biology, Stanford University, Stanford, CA, USA

[8]Howard Hughes Medical Institute, University of California, San Francisco, CA 94158, USA

[9]Correspondence to: mbarna@stanford.edu

Abstract

An outstanding mystery in biology is why some species, such as the axolotl, can regenerate tissues while mammals cannot[1]. Here, we demonstrate that rapid activation of protein synthesis is a uniquefeature of the injury response critical for limb regeneration in the axolotl (*A. mexicanum*).

By applying polysome sequencing, we identify hundreds of transcripts, including antioxidants and ribosome components are selectively activated at the level of translation from pre-existing mRNAs in response to injury. In contrast, protein synthesis is not activated in response to non-regenerative digit amputation in the mouse. We identify the mTORC1 pathway as a key upstream signal that mediates regenerative translation in the axolotl. Surprisingly, we discover unique expansions in mTOR protein sequence among urodele amphibians. By engineering an axolotl mTOR (axmTOR) in human cells, we show that these changes creates a hypersensitive kinase that allows axolotls to maintain this pathway in a highly labile state primed for rapid activation. Importantly, this change renders axolotl mTOR more sensitive to nutrient sensing. In support of this notion, inhibition of amino acid transport is sufficient to inhibit tissue regeneration. Together, these findings highlight the unanticipated impact of the translatome on orchestrating the early steps of wound healing in highly regenerative species and provide a missing link in our understanding of vertebrate regenerative potential.

Restoration of damaged tissues is the biggest biomedical challenge of this century. Most mammals have limited regenerative potential whereas urodele amphibians (newts and salamanders), and the axolotl in particular, canregenerate organs, including limbs, hearts, and brains, throughout their lifespan[1]. The mechanisms underlying this diverse regenerative potential are poorly understood. Our current understanding of regeneration is based on the transcriptome and not on direct assessment of proteins that are ultimately required for tissue regeneration[2–5]. However, axolotl genes are on average 25x longer than human[6]. *De novo* transcription and processing of these expanded transcripts may not be sufficient to guide rapid responses, such as wound closure after limb amputation, which occur within hours of injury. Therefore, a better understanding of molecular programs influencing gene expression in rapid wound healing is needed and is highly relevant to treating injury, organ failure, and disease.

Here we integrate translation profiling technologies with experiments in regenerative and non-regenerative species to discover a post-transcriptional gene expression program guiding wound closure and regeneration. These findings pinpoint rapid 'on-demand' translational remodeling of distinct gene networks, which may be particularly important for injury repair and promoting regeneration. We further identify mechanistic target of Rapamycin (mTOR) as a critical regulator, of this translational program, with an essential function in tissue regeneration. Moreover, our data reveal that evolution of the mTOR protein, within urodele amphibians creates a 'hypersensitive' kinase that extends its range of function and sensitivity. This uncovers the unexpected impact of highly conserved, key signaling pathways to be remodeled to foster differential regenerative potential across animal kingdoms.

Amputation activates protein synthesis

In axolotls rapid migration of epithelial cells scarlessly seals the wound within a day of limb amputation (Fig. 1a; Extended Data Fig. 1). In contrast, in non-regenerative species wound closure takes days, often resulting in extensive scarring (Extended Data Fig. 2a-b)[1]. Scarless wound closure paves the way for a signaling-competent wound epithelium (WE)

which stimulates the formation of a blastema – a stem-cell like progenitor pool that develops into a new limb (Fig. 1a)[1]. To examine how protein synthesis changes in response to injury, we employed sucrose gradient fractionation to separate mRNAs based on their ribosome occupancy, providing a snapshot of translation in the tissue at the site of limb amputation (Fig. 1b-c). Gradient traces from tissue harvested at 0 hpa (hours post amputation) had pronounced monosome (1 ribosome per transcript) peaks and a flat "heavy polysome" (3+ ribosomes per transcript) region indicating relatively low basal translation (Fig. 1b, d). Surprisingly, tissues harvested at 24 hpa were characterized by a reduced monosome peak and appearance of "heavy polysome" peaks indicating increased protein synthesis (Fig. 1c-d). This response is particularly notable as there are no changes in proliferation before 2 days post-amputation (dpa) (Fig. 1e-f)[7], suggesting that increased protein synthesis, at this time point, is not simply due to new cells being produced in the course of regeneration.

To better understand whether increased translation is specific to axolotls, we performed non-regenerative proximal amputations of digit 2 in mouse pups at postnatal day 7 (P7) (brown arrow in Extended Data Fig. 2a). At 0 hpa, the sucrose gradient trace exhibited prominent monosome and heavy polysome peaks suggestive of moderate translation. Notably, unlike the axolotl, the sucrose gradient traces of mouse digit tip tissue at 24 hpa were indistinguishable from the 0 hpa time point (Fig. 1g-i). These findings reveal a striking difference in protein synthesis at the site of amputation between regenerative versus non-regenerative injuries.

To visualize which tissues responded to amputation by increasing translation, we injected axolotls with O-propargyl-puromycin (OPP), which incorporates into nascent proteins and can be detected on tissue sections. We observed moderate OPP incorporation throughout the limb prior to amputation (0 h). However, at 2 hpa, we observed a global increase in OPP incorporation in all tissues of the amputated limb, including muscle, bone and connective tissue. This increase was evident in the newly formed wound epithelium (WE) formed by migration of epithelial cells over the cut site (Fig. 1j-k) and the skin near the wound site (labelled with cytokeratin), where it remained significant even at 24 hpa (Fig. 1l-m). In muscle (labelled with myosin heavy chain), the trend was maintained but was not significant at the 24 hpa time point (Fig. 1n-o). These findings indicate that injury leads to a broad increase in protein synthesis across multiple tissues in the axolotl. In contrast, *in vivo* OPP incorporation studies revealed that wildtype mice do not exhibit any overt differences in protein synthesis at 0 h, 2 h or 24 h after non-regenerative proximal digit amputation (Fig. 1p-r).

In the mouse, distal digit tip amputations that spare the nail bed can regenerate (Extended Data Fig. 2a-b) and rely on the presence of a stem cell niche[8]. In contrast, axolotl limb regeneration does not rely on a dedicated stem-cell pool and is therefore a distinct regenerative context[9]. While mouse regenerative distal digit-tip amputations do not trigger a global change in protein synthesis (Extended Data Fig. 2c-d), we did notice a significant and highly localized increase in OPP incorporation at 1 dpa that was spatially restricted to the skin adjacent to the cut site (Extended Data Fig. 2c (inset), e). This localized protein synthesis was accompanied by increased proliferation throughout the digit (Extended Data Fig. 2f-g). Notably, wound closure takes up to 1 week in the mouse (Extended Data

Fig. 2b). However, using OPP assays, we do not see evidence of increased translation or proliferation during re-epithelialization at 4 dpa (Extended Data Fig. 2h-k). Collectively, these data support the idea that activation of protein synthesis may be an important facet of regeneration and emphasize that a tissue-wide, global increase in protein synthesis, that is independent of proliferation and stem cells, distinguishes regenerative responses in axolotls and mice.

Injury triggers rapid translation

To determine which mRNAs are translated in response to limb amputation, we developed an axolotl-specific polysome sequencing pipeline (see Methods). In our approach, transcripts associated with the "free/ribonucleoprotein (RNP)", "light" and "heavy" polysome fractions were fractionated and sequenced from tissues harvested at 0 and 24 hpa and compared to transcripts from total lysate ("input") (Fig. 2a). We identified 8,139 mRNAs with detectable reads across samples (Supplementary Data 2). Consistent with our observation of increased protein synthesis, 17.3% of transcripts showed a greater than two-fold increase in heavy polysome association, indicating increased translation (Extended Data Fig. 3a). For half of these transcripts, greater polysome association was related to an overall increase in their transcript abundance after amputation (Extended Data Fig. 3b). To identify transcripts that were selectively translated in response to amputation independent of their transcription status, we calculated the change in translational efficiency (TE) of each mRNA (see Methods). We identified 504 transcripts that showed a two-fold increase in their TE, but no change in their transcription, between 0 and 24 hpa (green dots in Fig. 2b-c; Extended Data Fig. 3b). These transcripts are particularly interesting because they represent pre-existing mRNAs that are recruited to the ribosome in response to injury as seen by a drop in enrichment in the free/RNP fraction but no change in overall transcript abundance (Extended Data Fig. 3c-d). This suggests that increased translation of pre-existing mRNAs occurs in response to amputation. Moreover, because they do not change significantly in transcript abundance, these transcripts have been overlooked by traditional transcriptome analyses.

When we overlaid our data with a single-cell RNA-Seq data set[10], we observed that more than 50% of translationally activated ("TE UP", green dots in Fig. 2b-c, see table in Fig. 2c for FDR) mRNAs are associated with epidermal cells (including cells of the intermediate and basal wound epidermis shown in light green and small secretory cells and Leydig cells shown in dark green in Extended Data Fig. 3f). Conversely, more than one third of transcriptionally activated ("mRNA UP", orange dots in Fig. 2b-c) transcripts were derived from immune cells (with Gene Ontology (GO) enrichment for terms associated with immune responses (Fig. 2b orange; Extended Data Fig. 3g; Supplementary Data 3).Conversely, mRNAs with decreased abundance are associated with tissue-specific development and may be a hallmark of dedifferentiation (Extended Data Fig. 3h). The mRNAs that show no change in abundance or TE after amputation were highly enriched in regulators of "signaling" and "development", suggesting that these transcripts are not deployed until wound closure is completed (Fig. 2b grey; Extended Data Fig. 3i; Supplementary Data 3)[3,9]. Of note, the "TE DOWN" gene set did not show any significant enrichment of GO terms with the caveat that >66% of the mRNAs were not annotated ("TE DOWN" dark green dots in Fig. 2b; Supplementary Data 3). Broadly, these findings

highlight that translation and transcription target distinct biological processes in response to amputation.

To gain insight into the biological processes involved in wound healing, we conducted GO enrichment analysis on our set of translationally activated pre-existing mRNAs. To our surprise, these transcripts were highly enriched in GO terms associated with protein synthesis itself (Fig. 2b-c green; Extended Data Fig. 3j; Supplementary Data 3). For example, the "translation" GO term included multiple ribosomal proteins (RPs), translation initiation factors and t-RNA ligases (Fig. 2h inset, Supplementary Data 2). It is well-established that translation of many RPs and translation initiation factors is directly regulated by complex 1 of the mTOR pathway through pyrimidine-rich translational element (PRTE) and 5′ terminal oligopyrimidine tract (TOP) motifs encoded in the 5' leader sequences of their mRNAs[19,20]. We identified 101 axolotl orthologues of established mammalian mTORC1 targets (Supplementary Data 4) in our data set and observed that they are disproportionately enriched within the set of mRNAs that show a change in TE after amputation (Extended Data Fig. 3k)[19,20]. Therefore, activation of mTOR signaling may be an important contributor to translational remodeling upon amputation.

The top 20 translationally upregulated transcripts included key regulators of cellular redox state of which a subset was validated to show an increase in protein expression upon limb amputation (Extended Data Fig. 4a-b). Thioredoxin (TXN), which is expressed in the WE after amputation, plays an important role in disulfide bond reduction and negative regulation of reactive oxygen species (ROS), its downstream target peroxiredoxin (PRDX1) regulates hydrogen peroxide levels[11], and SELENBP1a (methanethiol oxidase) generates hydrogen peroxide in the process of oxidizing methanethiol[12] (Fig. 2b-c green, Supplementary Data 2, Extended Data Fig. 4a-b). The translational control of ROS regulators is of great importance as their fluctuation at sites of injury is required for regeneration in a variety of species, including zebrafish, frogs, planaria, and axolotls[13–16]. Selective translation of redox-regulating proteins suggests that a delicate balance of ROS during wound healing and regeneration is a part of a heretofore unexplored and tightly regulated post-transcriptional regulatory process. We also observe skin-specific protein upregulation of annexin A1 (ANXA1) which has been implicated in inflammation, phagocytosis, regulation of epithelial-to-mesenchymal transition and cell proliferation in cancer (Extended Data Fig. 4a)[17]. Our data also show that a key regeneration regulator, anterior gradient protein 2 (AGR2), is selectively translated as early as 48 h post-amputation, indicating that it may also play a role in early wound healing (Supplementary Data 2, Extended Data Fig. 4b)[2,10,18].

Amputation activates mTOR signaling

mTOR activation stimulates quiescent stem cells[21] and has been observed during the proliferative phases of zebrafish, axolotl and planarian regeneration[7,22,23]. However, mTOR activation during the early wound healing phase has not been reported in axolotl. The mTOR pathway integrates an array of environmental cues such as nutrient abundance, oxygen levels, growth factors and stress, to regulate cellular growth and metabolism. The serine/threonine kinase mTOR forms the catalytic core of two distinct complexes, mTORC1 and mTORC2[24]. Activation of mTORC1 triggers phosphorylation of two sets of

translational regulators, S6Ks (p70 S6 kinase 1 and 2) and 4E-BPs (eukaryotic initiation factor 4E-binding proteins 1, 2 and 3)[25,26]. Phosphorylation of S6K1 activates its kinase activity and it, in turn, phosphorylates ribosomal protein S6 (RPS6) at five highly conserved sites (Ser235, 236, 240, 244 and 247), which are used as markers of mTORC1 activation[27]. Western blot analysis of axolotl tissue harvested from the wound site between 0 and 24 hpa demonstrated a linear increase in phosphorylation of both Ser[235/236] and Ser[240/244] residues between 2 hpa and 24 hpa (Fig. 3a-b, Extended Data Fig. 5a-c, Supplementary Data 1). Of note, while Ser[235/236] may be phosphorylated in both an mTORC1-dependent and independent manner, the phosphorylation of the other residues depends exclusively on S6K1 and its homologue S6K2[27,28], demonstrating that amputation of the axolotl limb robustly activates the mTORC1 pathway. Notably, we observe phosphorylation of RPS6 throughout the tissue with elevated levels in the skin and WE, mirroring the pattern of OPP incorporation (Extended Data Fig. 5d-h).

While phosphorylation of RPS6 serves as a sensitive marker of mTORC1 pathway activation, its role in translation remains unclear[27]. Conversely, phosphorylation of 4E-BPs by activated mTORC1 plays a critical role in regulating protein synthesis[26]. In its native state, unphosphorylated 4E-BP1 sequesters the cap-binding protein eIF4E, thereby inhibiting translation. Phosphorylation of 4E-BP1 releases eIF4E to form the translation initiation complex and stimulates 5' cap-dependent translation[26,29]. We observe a significant increase in 4E-BP1 phosphorylation between 12 hpa and 24 hpa (Fig. 3c-d, Extended Data Fig. 5i-l). These data suggest that the spike in protein synthesis observed during wound closure may be directly regulated by mTORC1.

To test this hypothesis we treated axolotls with INK128 (MLN0128), a potent ATP-site specific inhibitor of mTOR[19]. Compared to controls (untreated or DMSO carrier control), axolotls treated with INK128 showed robust inhibition of RPS6 and 4E-BP1 phosphorylation within 4 h of drug treatment and failed to activate the mTORC1 pathway in response to limb amputation (Fig. 3e-i). Sucrose gradient fractionation of tissue harvested from the wound site revealed a profound decrease in translation in INK128-treated animals compared to DMSO-treated controls at 12 hpa (Fig. 3j). These data indicate that the increase in protein synthesis observed after amputation is partly dependent on mTOR activity. To assess if selective translation of pre-existing transcripts was dependent on mTORC1, we performed western blot analysis on tissues harvested from INK128-treated animals at 0, 24 and 48 hpa. We observed a significant decrease in the protein levels of known mTORC1-targets, Rpl19 and Rpl7a[19,20], at 48 hpa in drug-treated animals compared to controls. We did not observe a significant change in the levels of TXN, AGR2, SELENBP1, or ANXA1 in response to INK128 (Fig. 3k-l). This suggests that selective translation encompasses both mTORC1-dependent and independent mechanisms.

mTOR drives healing and regeneration

To determine the role of mTORC1 signaling in axolotl wound closure we examined the effect of INK128 treatment on wound healing after limb amputation. INK128 is an extremely selective ATP site mTOR inhibitor, which unlike Rapamycin, a first-generation mTOR inhibitor, has the ability to inhibit the 4EBP1 arm of the mTORC1 pathway which

has been shown to directly regulate protein synthesis[30–32].. Treatment with INK128 was associated with profound deficits in wound closure in 87.5% of drug-treated axolotls at 24 hpa. In contrast, 100% of controls (both untreated and those treated with DMSO carrier control) exhibited complete wound closure (Fig. 4a-b). Treatment with INK128 impaired epidermal cell migration between 30 min and 90 min after amputation (Fig. 4c-e; Supplementary Video 1 (control); Supplementary Data Video 2 (INK128-treated)). Notably, high doses of Rapamycin, also suppresses wound closure at 6 hpa likely through its effect on translation of 5' TOP containing mRNAs (Extended Data Fig. 6a-d)[19–20]. These findings, employing two different mTOR inhibitors, demonstrate that mTORC1 activation is critical for rapid wound closure.

Treatment with mTOR inhibitors such as INK128 does not distinguish between mTORC1 or mTORC2 inhibition which are both activated in the context of axolotl limb regeneration (Extended Data Fig. 5m-n). To assess whether the wound closure effects of INK128 were at least in part due to inhibition of mTORC1 dependent control of protein synthesis, we treated the animals with 4EGI-1 - a translation inhibitor which selectively disrupts binding of eIF4G and promotes binding of 4E-BP1 to eIF4E. In doing so, 4EGI-1 directly and specifically recapitulates inhibition of the 4E-BP1 arm of the mTORC1 pathway[33]. We observe that treatment with 4EGI-1 elicits the same wound closure defects as treatment with the mTOR inhibitor INK128 thereby suggesting that translational activation (which is regulated by mTORC1 and not mTORC2) plays a dominant role in this process (Fig. 4e-f).

Our polysome sequencing, detected translational activation of peroxiredoxin, an important antioxidant, within 24 hpa. Previous studies showed that sustained accumulation of ROS is critical for tissue regeneration[13,14,16]. In contrast, high levels are toxic, therefore cells must carefully orchestrate a balance of ROS production[34]. Importantly, when axolotls are treated with apocynin (APO), a drug that reduces ROS production, we observe the formation of a smaller blastema and delayed limb regeneration (Extended Data Fig. 6e-f). To address whether inhibition of mTOR activity impacts the ROS balance *in vivo*, we used 2',7'-dichlorodihydrofluorescein diacetate (H_2DCFDA) to detect ROS levels in INK128 or DMSO-treated limbs at 36 hpa (Fig. 4g-h). In DMSO-treated limbs at 36 hpa we observed that while all cells contained ROS, a subset of cells dispersed both in the epidermis near the wound site and in the WE had elevated ROS levels (Fig. 4h, Extended Data Fig. 6g). Upon treatment with INK128, we observed a significant increase in the intensity of H_2DCFDA at 36 hpa which suggested that inhibition of mTORC1 resulted in an increase in ROS at the wound site (Fig. 4h-i). Together, these results indicate that mTOR activation influences key aspects of the early tissue regenerative response such as wound closure and appropriate accumulation of ROS.

We further observed that even transient effects on mTOR signaling had long-term effects on regeneration. For example, the animals which responded to a single dose of INK128 with partial wound closure at 24 hpa, developed further tissue regression between 4 and 7 dpa and delayed induction of a blastema compared to controls (Fig. 4a; Extended Data Fig. 6h). We further allowed axolotl limbs to undergo complete wound closure before treating the animals with INK128 at 4, 6, 8 and 10 dpa (Fig. 4j-k). Treatment with INK128 after wound closure led to tissue regression at 14 dpa. Furthermore, at 28 dpa, all INK128-treated

animals remained arrested at the blastema stage while the controls had well-developed limb buds with distinct digit rays (Fig. 4k). This indicated that sustained mTOR signaling is required not only to drive initial wound closure immediately after injury, but also to maintain tissue integrity and sustain blastema formation during the proliferative stage. Notably, the drug-treated animals were able to re-initiate regeneration and form digits between 42 and 56 dpa likely due to subsequent re-activation of the mTOR pathway.

Hypersensitive mTOR drives regeneration

To determine if amputation-induced activation of mTORC1 is a general response observed in vertebrate wound healing, we examined the status of mTORC1 signaling in digit tips of neonatal mice after non-regenerative digit amputation as described in Fig. 1. Western blot analysis of digit tip tissue in mice revealed that mTORC1 signaling is not increased over basal levels in response to injury at 2 hpa and 24 hpa (Fig. 5a-b; Extended Data Fig. 7; Extended Data Fig. 8a-b) suggesting that mTORC1 activation, and concomitant increase in protein synthesis, are not a universal response to amputation and appear to be specific to the regenerative context.

To understand where the difference between axolotls and mice arises, we examined the mTORC1 pathway itself. It has been established that in the presence of nutrients, mTORC1 is recruited to the lysosomal membrane via the Rag-Ragulator complex where it is activated by RHEB and phosphorylates its substrates (Extended Data Fig. 8c)[35,36]. The components of this cellular machinery are highly conserved with axolotl proteins exhibiting an average of ~88% amino acid identity to their human and mouse orthologues (mTOR, RAPTOR, MLST8, LAMPTOR1–5, RAGA, RAGC, RAGD and RHEB) (Supplementary Data 5). However, we noticed an interesting feature when we examined the intracellular distribution of endogenous mTOR within tissues. In the mouse limb, at homeostasis, the mTOR staining appears diffuse and cytoplasmic (as shown in muscle in Fig. 5c). In contrast, axolotl mTOR localizes to lysosomes across multiple cell types (Fig. 5c, Extended Data Fig. 8d-e)[35,36]. This suggests that, in contrast to mammalian cells, a pool of axolotl mTOR remains constitutively localized to the lysosome potentially priming this pathway for rapid activation.

Although mTOR is highly conserved, to understand if there are specific features exclusive to axolotl mTOR, we performed a multiple sequence alignment across >100 metazoans, predominantly vertebrates, including 9 species of urodele amphibians (Supplementary Data 6-7). This analysis revealed that while axolotl mTOR is highly conserved (~84 % amino acid identity compared to both its human and mouse orthologues) (Supplementary Data 5), it contains two intriguing insertions embedded within otherwise highly conserved and functionally important M-HEAT regions encoded by exon 20 and 21 of mTOR (Fig. 5d). Insert 1 is an ~8 residue sequence within the M-HEAT region of axolotl mTOR which is critical for RHEB-mediated activation[37]. Structure modelling of human mTORC1 (PDB 6BCU) suggests that Gln57 within insert 1 may make a new direct contact with RHEB at Y67 of its Switch II domain, which is one of only four amino acids critical for activating mTORC1 (Fig. 5e)[37]. Notably, while this insertion is highly conserved across all three extant orders of amphibians (frogs, caecilians and salamanders), it is expanded by 6 residues in frogs. In addition, reptiles appear to encode a distinct insertion at this locus. The insertion

is otherwise absent across metazoans and the mammalian sequence appears to be ancestral as it is also found in invertebrate species. In contrast, insert 2 is a ~20 residue insertion, within the M-HEAT domain, which is remarkably found exclusively in urodele amphibians (Fig. 5d, f-g, Supplementary Data 6-7). This insertion extends the M-HEAT and N-HEAT interface between two mTOR proteins in the mTOR dimer, predicted to play a role in mTOR dimerization (Fig. 5f-g)[38]. To assess the impact of these insertions, we used CRISPR/Cas9-mediated gene editing to engineer a chimeric human-axolotl mTOR by incorporating the two contiguous axolotl insertions in frame into the human mTOR genomic locus (axmTOR) to generate homozygous HEK293T[axmTOR] cell lines (Fig. 5d boxed sequence; Extended Data Fig. 9a-c). Subsequent nutrient deprivation experiments revealed that in HEK293T[axmTOR] cells, mTOR localization to lysosomes is less sensitive to starvation than in the wildtype HEK293T and that a pool of mTOR persists at lysosomes of HEK293T[axmTOR] cells, similar to what we observe in the axolotl (Extended Data Fig. 9d-e; Fig. 5c).

We hypothesized that axolotl insertions may alter the behavior of mTOR kinase. It is established that mTOR is activated upon nutrient and amino acid stimulation[35,36]. Notably, nutrient signaling has been suggested to play an important role in tissue regeneration[39–41]. By carrying out amino acid titration experiments, we show that HEK293T[axmTOR] cells are more sensitive to changes in nutrient levels and respond to subtle changes in amino acid concentration by incrementally regulating the phosphorylation of 4EBP1 and RPS6 (Fig. 5h-i, Extended Data Fig. 10a-d). HEK293T[axmTOR] cells are also better able to discern differences in duration of exposure to nutrients by modulating phosphorylation of mTOR substrates (Fig. 5j-k; Extended Data Fig. 10e-f). Furthermore, the axmTOR has the remarkable ability, upon amino acid titration, to not exceed the upper limit of activation of the human mTOR. These findings suggest that the axmTOR is distinct and is not functioning in the same capacity as a wildtype or an oncogenic mammalian mTOR kinase. Intriguingly, this notion is consistent with the axolotl's capacity to regenerate while possessing extraordinary resistance to oncogenic transformation[42,43]. Next, a viability assay revealed that the axmTOR kinase is a 'hypersensitive kinase' as upon INK128 treatment it exhibits a significantly lower IC50 than its human counterpart (Fig. 5l). These findings suggest that axolotl-specific insertions allow axolotl cells to maintain an increased dynamic range of mTOR sensitivity to more rapidly and robustly respond to nutrient and metabolite changes underlying regeneration.

To extend our understanding of why axolotl mTOR is distinct, we looked to our structure models. Our model suggests that the urodele-specific insert 2 may create a novel "bridge" between two mTOR monomers thereby stabilizing the mTOR dimer. This is significant because dimerization is necessary for mTORC1 assembly, localization to the lysosome and RHEB binding[44,45]. We observed that at steady state axmTOR binds significantly more RHEB than wildtype mTOR suggesting that it preferentially exists as a fully assembled mTORC1 (Fig. 5m-n). This would account for our prior observations of hypersensitivity to nutrients and constitutive localization to the lysosome as both of these functions rely on the fully assembled mTORC1 complex. To test whether this priming also extends to translational responses, we assessed the translation status of previously identified mTOR-sensitive mRNAs that are also activated upon amputation in the axolotl. We observed a significant increase in translation of RPL19a and a trend of activation in CIRBP (Cold-

inducible RNA-binding protein) (Extended Data Fig. 10g-i) in HEK293T[axmTOR] cells. These findings suggest that the distinct axmTOR structure may be sufficient to not only alter nutrient sensitivity but also confers a primed translational state.

To understand how injury might trigger activation of the hypersensitive axolotl mTOR, we considered that nutrients are potent regulators of mTOR and previous studies have implicated nutrient signaling in regeneration[39–41]. Therefore, we tested the hypothesis that nutrients (i.e. amino acids) released from cells at the site of injury, might be sufficient for regenerative mTOR activation and tissue regeneration. To test this,we treated axolotls with an inhibitor (V-9302) of the glutamine transporter ASCT2/SLC1A5[46]. ASCT2 establishes a glutamine gradient which is used by its partner LAT1/SLC7A5 to import essential amino acids into the cell by exchanging them for glutamine. This glutamine flux has been directly implicated in mTOR activation, particularly in cancer[47]. Notably, the mRNA levels of both ASCT2 and LAT1 increase at 24 hpa in the axolotl implicating these amino acid transporters in the healing process (Fig. 5o-p). Strikingly, treatment with V-9302 prevented wound closure in all animals at 24 hpa (Fig. 5q-r). Collectively these findings suggest that urodele amphibians may rely on a hypersensitive mTOR to detect low levels of amino acids in the wound microenvironment. Therefore, the functional differences in upstream regulation of protein synthesis control, through mTOR sequence differences between species, may underlie the remarkable ability to repurpose a classic 'stress-response' signal to a 'growth and regeneration' signal.

Discussion

In this study, we show that upregulation in protein synthesis is a key feature of tissue regeneration. We further reveal a hidden repertoire of hundreds of pre-existing transcripts that are rapidly recruited to ribosomes in response to amputation. These findings serve as a springboard for future studies aimed at identifying the functional roles of these transcripts in regeneration, with one important class associated with ROS activation. We further show a critical role of mTOR signaling in the translation control response, wound healing, and regeneration. In addition, we demonstrate that axolotls encode a hypersensitive mTOR kinase that exists in a state primed to sense incremental changes in extracellular cues and to promote rapid translation of pre-existing mRNAs.

Given the known trade-off between high metabolic activity and regenerative potential, it is possible that changes in this key metabolic regulator may have impacted the evolutionary trajectories and adaptions of amphibians.[48] The comparatively low sensitivity and narrow dynamic range of mammalian mTOR suggests that it may not discern or respond to activating cues associated with injury. It has been suggested that nutrient cues, including insulin and leucine, may promote regeneration in a variety of species[39–41,49]. As leucine in particular is a powerful stimulator of mTOR[50], this suggests that increased sensitivity of this pathway in the axolotl may have a rapid and direct beneficial effect in coupling nutrient sensing with gene expression at the post-transcriptional level to initiate and sustain regeneration. Indeed, we have found that amino acid transport at the time of injury, is necessary for axolotl wound closure. These findings further suggest the possibility that

engineering an axolotl-like mTOR activity may allow us to promote wound healing, and perhaps even tissue regeneration, in mammals without triggering oncogenic transformation.

Methods

Animal experimentation

All experiments using axolotls or mice were approved by Stanford University's Administrative Panel on Laboratory Animal Care (APLAC). Axolotls were housed in 40% Holtfreter's Salt Solution ("tank water") at room temperature. Axolotls were anesthetized before any procedure involving amputation, injection or live imaging using Tricaine dissolved in 40% Holtfreter's Salt Solution at the following concentrations titrated based on body size (0.25 g/L for animals 3–8 cm snout to tail tip, 0.5 g/L for 8–12 cm animals, 1 g/L for 12–15 cm animals and 2 g/L for 15–19 cm animals). Experiments were performed at 16–20°C. Axolotls recovered in 0.5 mg/L butorphanol tartrate dissolved in clean tank water for 24 h after the procedure. Animals were euthanized following APLAC approved procedures (axolotls in 5 g/L Tricaine; mice via CO_2 exposure). Axolotl limb amputations were performed through the left forelimbs at the mid-forearm level. Mouse proximal digit-tip amputations were performed at the level of P1/2. Distal digit-tip amputations were performed at the level of P3. All procedures on animals (axolotls and mice) were performed following APLAC approved protocols. No sample-size calculation was performed. Sample sizes for all experiments are indicated in the Methods beolw or Figure legends. All n's refer to independent biological replicates unless otherwise specified. Animal experiments were performed on multiple unique animals from individual cohorts (exact n's are specified in the Figure legends). Animals were randomly assigned a numerical identifier by animal facility staff and experimenters allocated them treatments based on these randomly assigned numbers. Blinding was not feasible.

OPP Incorporation and Immunofluorescent Staining

O-Propargyl Puromycin (OPP) was purchased from Medchem Source LLP (25mg, JA-1024), reconstituted in sterile DMSO (100 mM final concentration), aliquoted and stored at −80°C. Prior to injection, OPP aliquot was further diluted in DMSO (Sigma) to a working concentration of 10 mM (4.9553 mg/mL). Animals were anesthetized, weighed and underwent amputation as described. OPP was injected intraperitoneally 1h prior to tissue harvest at 0 h, 2 h, or 24 h post-amputation. Injection aliquots were prepared by combining appropriate volume of 10 mM stock and 0.8x sterile PBS for axolotls (or 1x sterile PBS for mice) adjusted to a pH of 6.5[51]. Next, 0.49553 mg of OPP was administered per 20 g body mass. An injection volume of 100 µL was used. After 1 h, animals were euthanized following APLAC approved protocol. Tissue was harvested and fixed for 1 h at 4°C in 4% paraformaldehyde in PBS. For all washes, 0.8x PBS was used for axolotl tissues and 1x PBS was used for mice. The tissues were washed 4x for 15 min at 4°C. The first wash was in PBT (PBS, 0.1% Tween), subsequent washes were in PBS. Samples were equilibrated in 30% sucrose solution in filtered 0.1 M potassium phosphate buffer at 4°C overnight, and for 1 h in Tissue-Tek O.C.T. (Sakura Finetek, #24583) in molds. Samples were frozen on dry ice. Tissues were sectioned, equilibrated to RT (room temperature) for 1h and rehydrated for 1 h in blocking buffer (PBS with 1% goat serum and 0.1%

Triton-X) and incubated overnight, at 4°C, with primary antibody against cytokeratin 5/6/18 (Santa Cruz Biotechnology, sc-53262) or myosin heavy chain (DSHB, MF-20) at 1:50 dilution in blocking solution. Slides were washed three times 15 min in blocking buffer and incubated with secondary antibody conjugated with Alexa Fluor 488 or Alexa Fluor 568 (Thermo Fisher, A-11017 or A10037) at 1:500 dilution and DAPI at 1:1000 dilution in blocking buffer for 1h in the dark at RT. Slides were rinsed twice in blocking buffer for 15 min and twice in PBS for 5 min. The Click-iT Alexa Fluor Picolyl Azide Toolkit was reconstituted, and components were combined per manufacturer's instructions (Thermo Fisher C10641 or C10642). Components C and D were combined in a 1:4 ratio. Slides were rinsed twice in PBS for 5 min and 150 μL of reaction cocktail as added per slide. Slides were incubated for 30 min in a humidified chamber in the dark, at RT. They were then rinsed twice for 5min in PBS and coverslips were mounted with Fluoromount-G Slide Mounting Medium (Southern Biotech, 0100–01). Slides were imaged on a Zeiss Axio Observer Z1 microscope coupled to the Perkin Elmer UltraVIEW Vox spinning disk confocal microscopy system and images were acquired with Volocity. Images were quantified using ImageJ. Mean fluorescence intensity was measured within a manually defined region of interest (ROI) containing the digit at the plane of amputation (mice), skin (defined by cytokeratin staining) or muscle (defined by MHC) staining. Mean background fluorescence was also measured in an adjacent ROI lacking tissue and subtracted from the sample fluorescence. Mean fluorescence intensity of a given sample is the average of two ROIs normalized to the mean fluorescence intensity at 0 h post-amputation. In mice, proximal amputation was performed through P1/2, distal amputation was performed through P3. For analysis in mice n=3 (CD1 at P7) in Fig. 1r, individual animals were used for each time-point. In Extended Data Fig. 2, at least 3 individual animals were used for each analysis and time-point. For each time-point, the number of white axolotls (AGSC_101J812; 8–12 cm from snout to tail) used was n=9 (0 h), n=5 (2 h), and n=8 (24 h) were used. Significance was assessed using Whitney-Mann rank test for pairwise comparison, for comparison of more than two conditions, significance was assessed with a one-way ANOVA analysis.

For immunofluorescent staining shown in Figure 1, 5 and in Extended Data Figures 2, 4, 6 and 7, we followed the standard protocol described above but omitted the OPP administration and detection steps, and used primary antibodies against mTOR (Cell Signaling Technology, #2983S), Rab7 (Santa Cruz Biotech, sc-271608), TXN (Aviva, ARP72618) and ANXA1 (Proteintech, #21990–1-AP) diluted to 1:50 or P-RPS6$^{Ser240/244}$ (Cell Signaling Technology, #5364S) and phospho-histone H3 (Sigma-Aldrich, #06–570) diluted to 1:100. Alexa fluor conjugated secondary antibodies at 1:1001:500 dilution as described above. Slides were images on a. Images for OPP incorporation and PH3 staining in mouse shown in Extended Data Fig. 2, and PH3 incorporation in axolotl shown in Fig. 1e were acquired using widefield imaging on a Nikon TiE Spinning Disk Confocal. Images for TXN and ANXA1 staining shown in Extended Data Fig. 4 were acquired using an inverted Zeiss LSM780 confocal microscope. Images for OPP incorporation in mouse and axolotl shown in Fig. 1, as well as mTOR and Rab7 staining in Fig. 5 and Extended Data Fig. 8 were acquired using the UltraVIEW Vox spinning disc confocal system described above.

Sucrose Gradient Fractionation

Axolotl limb amputations were performed as described above. A ~2 mm piece of tissue was harvested at 0 h and at 24 h post-amputation, immediately frozen by direct immersion in liquid nitrogen and stored at −80°C until use. Samples were prepared by pooling and powderizing tissues in from 2–5 age-matched animals. Tissues were powderized in liquid nitrogen with a mortar and pestle. We prepared n=5 independent pools of tissues for each time-point from 5 wildtype subadults (AGSC_100S; 12–17 cm from snout to tail) for experiments in Figures 1 and 2. Wildtype juveniles (AGSC_100J812; 8–12 cm from snout to tail) were used for sucrose gradient fractionation experiments upon DMSO or INK128 treatment shown in Figure 3 where n=3 independent pools of tissue from pairs of animals were used for each treatment. For mouse sucrose gradients, n=3 independent pools of digit 2 tips were used per time-point harvested from CD1 pups at post-natal day 7. Dissociation and lysis of tissues was optimized for the axolotl as follows: powderized tissue was resuspended in lysis buffer (100 mM Tris pH7.5, 15 mM $MgCl_2$, 150 mM NaCl, 1% Triton X-100, 2 mM DTT, 750U/mL SuperaseIn RNase Inhibitor (Ambion, AM2696), 0.2 mg/mL cycloheximide (Sigma-Aldrich, C7698–1G), 1X Halt Protease and Phosphatase Inhibitor Cocktail (Thermo Fisher, 78442), 25 U/mL Turbo DNase (Thermo Fisher, AM2238), 8% Glycerol, 0.5% DOC, 0.5 mg/mL heparin, 200 U/mL RNaseOUT Recombinant Ribonuclease Inhibitor (Thermo Fisher, 10777019), 400U/mL RNasin (Promega, N2611) at 500 μL per 70 mg of tissue powder. High quantities of RNase inhibitors were used due to allow isolation of intact polysomes which were otherwise degraded by the high endogenous nuclease activity of axolotl tissues. Samples were incubated on ice for 20 min with sporadic vortexing and lysate was pipetted through a p1000 tip and p200 tip and then passed three times through a 16 G sterile needle and four times through an 18G needle to dissociate the tissue. It was then cleared by centrifugation (four times 5 min each at 4°C) at 5000 g. After clearing, the final volume was topped up to 500 μL if needed. For samples to be used for polysome sequencing (see below), 75 μL were removed, combined with 1 mL of Trizol Reagent (Invitrogen, 15596018) and stored at −20°C. The remaining lysate was loaded on 4 mL sucrose gradients (112.5 μL per gradient) and underwent centrifugation for 2.5 h at 4°C at 35,000 rpm on Beckman SW60 rotor. Sucrose gradients were prepared by sequentially layering and freezing 800 μL of 17.5%, 25.6%, 33.8%, 41.9% and 50% sucrose dissolved in 15 mM Tris-HCl pH7.4, 15 mM $MgCl_2$, 300 mM NaCl. Gradients were stored at −80°C and thawed overnight at 4°C prior to use. Gradients were fractionated using a density gradient fraction system (Brandel, BR-188). Quantitation was performed by baselining the gradients and calculating the area under the curve for the monosome and heavy polysome (3+ ribosomes) and normalizing it to the total area under the curve from the monosome to the end of the heavy polysome. Significance was assessed by Student's t-test with values considered significant when p<0.05. Gradient traces were systematically normalized as follows: first we identified the 'zero' point by identifying the first point where the detector read '0' that was followed by a reading of 24.563 (this value is a maximum system set point that occurs immediately after the '0' point on our unit upon detection of 60% sucrose causing readings to jump artificially). For all data < 1, we added 24.563 to the absorbance to correct the readings and allow a continuous shift from one side of the zero point to the other. For all data points >24.563 nothing was added. To move the corrected data back to the baseline, we identified the lowest absorbance measurement after '0' - this was specific for each sample

(i.e. 24.559) and subtracted this amount from all values bringing the baseline to 0. This value is the reading for 60% sucrose at the end of the run. The value of the peak (highest value) of monosome, disome and trisome were identified and the 'peak' point was used to calculate the mid-point distance between these regions and establish their boundaries. The area under the curve was then calculated and expressed as a percentage of the area under the curve exclusive of the RNP region.

Library preparation for Polysome Sequencing

To assess which transcripts are translated upon limb amputation in the axolotl, we developed an axolotl-specific polysome sequencing pipeline which optimized tissue harvest, lysis, sucrose gradient fractionation (as described above) and analysis. This was necessary because unlike humans and mice, axolotls express high levels of nucleases that make it challenging to capture intact polysomes under standard mammalian protocols. In addition, we could not reliably apply emerging ribosome-profiling methods[52] because of the size of the axolotl transcriptome[6,53] and the lack of characterized isoforms which precluded accurate mapping of short ribosome protected fragments (RPFs) to determine translation efficiency. Polysome sequencing[54] was performed on two biological replicates which were subjected to independent harvesting, library preparation and sequencing. For each replicate, we prepared an independent pool of tissues for each time-point each containing tissues from 5 wildtype subadults (AGSC_100S; 12–17 cm from snout to tail) and subjected them to sucrose gradient fractionation as described above. For each time-point lysate was divided across three 4 mL sucrose gradients and fractions were collected into tubes containing 100 μL of 10% SDS. Then 500 μL of each fraction was transferred to a tube containing 700 μL acid-phenol, 100 μL water and 100 μL sodium acetate. "Input" samples collected prior to fractionation as described above were combined with 1 mL of Trizol Reagent, 200 μL of chloroform and shaken for 15 s. Input samples were then incubated at RT for 2–3 min and 500 μL of the aqueous phase were transferred to a tube containing acid phenol, water and sodium acetate. After shaking/vortexing briefly, both input and fraction samples were allowed to rest at RT for 5 min and centrifuged at 13,200 rpm for 10 min at 4°C. Then, 400 μL of each fraction sample was combined with isopropanol and GlycoBlue. Samples were gently inverted and precipitated overnight at −80°C. The samples were then centrifuged at 13,200 rpm for 30 min at 4°C. The pellets were washed twice with 75% ethanol, air dried and resuspended in 10 μL (for fractions) or 40 μL (for input) of Ultra Pure DNase/RNase-Free Distilled Water (Invitrogen, 10977-015). For each time-point, the fractions were pooled into three tubes as follows: (1) RNP to 40S, (2) "light" polysome containing the monosome and disome fractions, (3) "heavy" polysome containing all fractions with 3+ ribosomes. The total volume was topped up to 181 μL with Ultra Pure water and 1 μL of the sample was used to check concentration. Then, 1 μL of 1:200 ERCC RNA Spike-In Mix (Invitrogen, 4456740) was added to each fraction pool and concentration was measured again. DNase treatment was performed with TURBO DNase (Ambion, AM2238) for 30 min at 37°C in a total volume of 500 μL. Samples underwent a second acid phenol extraction as described above, were resuspended in 30 μL of Ultra Pure DNase/RNase-Free Distilled Water. The libraries were prepared by the Stanford Genomic Services Center per manufacturer's instructions using the TruSeq Stranded Total RNA Library Prep with

Ribo-Zero Gold Human/Mouse/Rat (Illumina) and sequenced (PEx150) on a HiSeq 4000 (Illumina).

Analysis of Polysome Sequencing Data

Quality control of raw sequences was performed using FastQC (www.bioinformatics.babraham.ac. uk/projects/fastqc/). Adapters were clipped using Trimmomatic-0.36 with the following settings LEADING:5 TRAILING:40 MINLEN:50[55]. Reads with phred quality score > 33 were kept and FASTQC was repeated again to confirm quality of remaining reads. The axolotl transcriptome[5] was downloaded from https://portals.broadinstitute.org/axolotlomics/Axolotl.Trinity. CellReports2017.fasta and concatenated to the sequences of ERCC Spike-In mix sequences (Invitrogen, ERCC92.fa) and used to build a transcript to gene reference index with RSEM version 1.2.30[56]. Paired reads were aligned to the index with Bowtie 2 version 2.2.9[57] and expression was calculated with RSEM. The data set contained 1,388,890 gene models identified in the reference transcriptome. Of these, 473,373 had > 0 reads across all libraries. Normalization of raw read counts in the free/RNP, light and heavy polysome libraries was performed linear scaling to equalize ERCC reads across these libraries to the ERCC reads in the heavy polysome library at 0 h. Normalization of raw read counts in the free/RNP, light and heavy polysome libraries was performed linear scaling to equalize ERCC reads across these libraries to the ERCC reads in the heavy polysome library at 0 h. The approach was to spike in the same quanity of ERCC to each polysome fraction sample (i.e. free/RNP at 0h "RNP_0h", light polysome at 0h "light_0h" and heavy polysome at 0h "heavy_0h" and similarly for the 24 h samples). Our normalization approach is based on the assumption that since the same quantity of ERCC was spiked into each sample in a set (i.e. free/RNP at 0h "RNP_0h", light polysome at 0h "light_0h" and heavy polysome at 0h "heavy_0h" and similarly for the 24 h samples), these samples should yield equal numbers of ERCC reads after sequencing. Due to differences in amplification, samples will have different numbers of ERCC reads, therefore we selected one sample (heavy_0h) as the reference sample and we plot the abundance of ERCC reads in this sample on the x-axis and the abundance to ERCC in each of the other samples in a set in turn (i.e. RNP_0h) on the y-axis. The resulting equation describing this linear relationship in ERCC reads for 92 different ERCC "genes" is then applied to all the reads in the target sample (i.e. RNP_0h) as we assume that any differences in amplification affected ERCC reads to the same extent as target reads. This procedure is repeated for each sample (RNP_0h, light_0h, RNP_24h, light_24h, and heavy_24h). Each replicate is normalized separately to the ERCC reads in its own heavy_0h sample since in our case these were prepared and sequenced at different times. For the input libraries, the input_24h sample is normalized to the input_0h sample based on their ERCC reads. Each replicate's input samples are normalized to their own input_0h. We subset the data to retain transcripts with > 1 cpm across all the input libraries and > 10 reads in total across all RNP/free, light and heavy polysome libraries thereby retaining 8,139 transcripts that had > 0 reads across all libraries and replicates. Differential expression analysis was performed using the edgeR and limma packages[58,59]. The voom function was used to enable linear modeling of RNA-Seq data with limma[60]. Analysis was performed using the following design matrix (~0+group+batch) where group is the sample type (i.e. input at 0 h) and batch identifies the specific replicate. The following comparisons were defined in the

corresponding contrast matrix to compare the translational efficiency at the 0 h and 24 h time-point TE=((heavy24h-heavy0h)-(RL_24h-RL_0h)) where "heavy" denotes the average expression in the heavy polysome at the given time-point and RL denotes the average expression in the free/RNP (R) and light polysome (L) fractions at a given time-point. This is reported as " TE" in Supplementary Data 2. Change in mRNA abundance in the input at 0 h and 24 h was defined as (input24h-input0h) this is reported in the " mRNA abundance" field of Supplementary Data 2. Additional contrasts defined in the matrix included the change in enrichment in the free/RNP fraction relative to the other two fractions, defined as (RNP24h-RNP0h)-(LH_24h-LH_0h) where RNP refers to the average expression in the RNP/free fraction and LH refers to the average expression in the light and heavy polysome at a given time-point which was used to examine the correlation between TE and enrichment in the free/RNP fraction (log2FC free/RNP) shown in Extended Data Fig. 3c and reported as " RNP/free enrichment" in Supplementary Data 2. This metric was used to determine the Pearson correlation between change in TE and enrichment in the free/RNP fraction compared to the change in mRNA abundance as shown in Extended Data Figure 3c and 3d, respectively. We also calculated the enrichment in the light polysome defined as (light24h-light0h)-(RH_24h-RH_0h) where light refers to the average expression in the light polysome at a given time-point and RH is the sum of average expression in the free/RNP and heavy polysome fractions. This data was used when defining the subset of genes with "no change" in either the input or the free/RNP, light or heavy polysome fractions and depicted as grey dots in Figure 2b. Using the contrast matrices and experimental design described above, linear models were fitted to the data using limma-voom with empirical Bayes method. The p-values were adjusted for multiple-testing using the Benjamini-Hochberg procedure and the adjusted p-values (FDR) are reported for each gene in Supplementary Data 2. Note that in this table, "Gene" refers to the axolotl transcript annotation from the Bryant et al. (2018) assembly, whereas Uniprot, Gene_ID, Protein_Name, Gene_Name, Organism and Gene_Synonyms refer to gene annotations in the closest orthologous gene (for details see Bryant et al. 2018) across a wide-variety of organisms. Note that many genes do not have annotations and therefore have blank space or NA in these respective fields.

In Figure 2b and 2c (and Supplementary Data 2), the green dots highlight the TE UP (no mRNA) category (504 genes) defined as TE > 1 and | mRNA abundance| < 1; dark green dots highlight the TE DOWN (no mRNA) category (521 genes) defined as TE < (−1) & | mRNA abundance| < 1. The mRNA UP and TE UP category highlighted in pink is defined as TE > 1 and mRNA > 1 and contains 152 genes; the mRNA UP (no TE) category highlighted in orange contains 1190 genes and is defined as | TE| < 1 and mRNA > 1. The mRNA DOWN (no TE) category shown in blue is defined as | TE| < 1 and mRNA < (−1) and contains 156 genes; lastly the no change category highlighted in grey contains 5,001 genes and is conservatively defined as all transcripts with | TE| < 1 and | mRNA| < 1 and | RNP/free| < 1 and | light polysome| < 1. Note that due to this stringency, there are some black dots within the grey region that are excluded by this definition.

The change in abundance of a given transcript in the heavy polysome ($\log_2$ fold change (FC) heavy polysome) is shown on the x-axis in Extended Data Figure 3a-b with the $\log_{10}$ adjusted p-value (p_{adj}) plotted on the y-axis. Note that the change in the heavy polysome

is a less informative metric, than change in TE (as shown in Figure 2b), to describe the translational regulation of a transcript. This is because while 17.3% of transcripts show a significant increase (p_{adj} <0.05) in their abundance in the heavy polysome after amputation (Extended Data Figure 3a), the increase for most is due to a concomitant increase in transcription as illustrated by the distribution of orange and pink dots representing transcripts that increase in their abundance in the input at 24 h post amputation in Extended Data Figure 3b. Whereas analysis of changes in TE clearly identifies transcripts that are upregulated solely at the level of translation (green dots in Extended Data Figure 3b and Figure 2b).

Gene ontology annotation

Biological function gene ontology annotation was carried out using the Database for Annotation, Visualization, and Integrated Discovery (DAVID, https://david.ncifcrf.gov/home.jsp) which integrates information from a variety of databases such as KEGG, UniGene and Gene Ontology, to provide comprehensive annotation of gene lists[61]. DAVID supports analysis of lists containing genes from a variety of species allowing us to directly use the data associated with orthologue annotations in the Bryant et al. (2018) axolotl transcriptome assembly. We extracted the Uniprot identifiers for orthologues of axolotl genes in each gene subset defined in Figure 2b-c and Supplementary Data 2, for example orange/ mRNA UP and green/ TE, and compared gene ontology enrichment within each of these sets to a "background" list comprised of Uniprot identifiers of orthologues of genes in the "no change" (grey) category stringently defined as transcripts that do not show change in the input, free/RNP, light or heavy polysome fraction over time. Figure 2e-h show the top 6 biological function categories enriched within each gene set and the full list of significantly enriched functional categories may be found in Supplementary Data 3. Significance was assessed in DAVID using the Benjamini and Hochberg method to determine p-values adjusted for multiple testing using a linear step-up approach[62]. An adjusted p-value < 0.05 was deemed statistically significant and is reported in Supplementary Data 3. Note that although the TE DOWN/no mRNA gene subset (dark green dots in Figure 2b) contains 521 genes, only 182 contained annotations and no significant gene ontology enrichment was observed relative to the background. Further, DAVID annotation and manual search were used to identify Gene Ontology categories associated with cell "signaling" or "development" (i.e. GO:0060173-limb development) and identified 1,995 genes within our data set that belonged to these categories. Next, we examined the distribution of these "signaling" and "development" genes across the TE and mRNA categories defined in Figure 2b. We observed that the majority (>76%) of these genes fell within the "no change" gene cluster (shown in grey in Figure 2b), an additional 14.3% of these genes belonged to the transcriptionally activated gene cluster (shown in orange in Figure 2b) whereas all other categories accounted for fewer than 10% of the remaining genes within the "signaling" and "development" cluster.

Cell type enrichment analysis

For cell type enrichment analysis, our data was overlaid with a previously published single-cell RNA-Seq analysis of wound healing and regeneration in the axolotl limb and leveraged axolotl gene annotations shared between the two data sets which were mapped to the same

transcriptome[10]. We identified 480/504 annotations for the TE UP/no mRNA (green) category and 1,020/1,190 for the mRNA UP (no TE) (orange) category and summarized their distribution across epidermal cell types (including intermediate wound epidermis, basal wound epidermis, Leydig cells and small secretory cells), immune cells (including T cells, early B cells, neutrophils, B cells, recruited macrophages and phagocytosing neutrophils), vascular system cells (including erythrocytes and endothelial cells), neural cells (including dendritic and Schwann cells) as well as fibroblast-like blastema cells.

mTOR-sensitive orthologue enrichment

To assess distribution of mTOR target genes in our data set, we identified previously described 189 genes shown to contain an-mTOR sensitive TOP or PRTE motif or to exhibit sensitivity to drugs targeting mTORC1 (Supplementary Data 4)[19,20]. We identified 79 unique axolotl orthologues of these mTOR-sensitive genes within our data set. An additional 11 mammalian mTOR-sensitive genes had two orthologues each in axolotls. The distribution of mTOR-sensitive orthologues across our data set was as follows: 101 mTOR-sensitive orthologues /8139 total genes; 57/5001 in the "no change" data set (grey dots in Figure 2b); 32/504 in the TE UP/no mRNA data set (green in Figure 2b); 1/521 in the TE DOWN/no mRNA data set (dark green in Figure 2b); 1/107 in TE DOWN/mRNA DOWN data set; 6/152 in the TE UP/mRNA UP data set (pink in Figure 2b); and 6/1,190 in the mRNA UP/no TE data set (orange in Figure 2b). To simplify analysis, these were distributed into three categories ("no change" containing 57/5001 genes, TE containing 40/1304 genes, and mRNA containing 9/1625 genes). The percentage of mTOR-sensitive orthologues within each of these three categories is shown in Figure 2i. Genes that showed changes in both translation and transcription (for example those in the "pink" category) were counted once in each of the above categories. An Exact binomial test was performed in R (binom.test where x was the number of mTOR-sensitive orthologues in a given category, n was the total number of genes in that category and p was the hypothesized probability of mTOR-sensitive genes in the data set to 101/8139) to assess the probability of a given mTOR-sensitive gene belonging to one of these three categories based on the expected probability. In the figure ** indicates $p < 0.001$, **** indicates $p \ll 0.00001$, n.s. indicates $p > 0.05$ and is not deemed statistically significant.

Western blot analysis of protein expression

Source images for all western blots are included in Supplementary Data 1. Axolotl limb or mouse digit-tip tissue was harvested as described above and immediately snap-frozen by direct submersion in liquid nitrogen. The samples were powderized with a mortar and pestle under liquid nitrogen or a TissueLyser II chilled to −80°C (Qiagen). The samples were lysed in RIPA buffer for 30 min on ice with intermittent vortexing (0.15M NaCl, 0.05M Tris-HCl pH7.4, 0.005M EDTA pH8, 0.001M EGTA pH8, 0.025M sodium pyrophosphate pH7.4, 0.001M sodium orthovanadate, 0.01M NaF, 0.001M B-glycerol phosphate, 0.1% SDS, 1% NP-40, 0.5% DOC and 1 tablet of cOmplete, Mini, EDTA-free Protease Inhibitor Cocktail (Roche, 11836170001) per 10mL of buffer supplemented with 1X Halt Protease and Phosphatase Inhibitor Cocktail (Thermo Fisher, 78442) prior to use) and cleared by centrifugation at 13,200 rpm at 4°C for 5 min repeated twice. Samples were sonicated with a Bioruptor Sonication System (Diagenode) on medium intensity with a 30 sec ON and

30 sec OFF cycle for 5 min and cleared one more time by centrifugation as described above. The protein concentration of cleared samples was determined with a Pierce BCA Protein Assay Kit (Thermo Fisher Scientific, #23225) with measurements conducted on a GloMax-Multi Plate Reader (Promega, E7081). Equal amounts of protein were diluted in 15 μL or 30 μL total volume with 1X Laemmli SDS-sample buffer (Fisher, 50–196-784), boiled at 95°C for 5 min, chilled on ice and loaded onto 4–20% polyacrylamide gels (Biorad #5671095, #4568096, #4561093, #5671094). The same gel size was used for all replicates of a given experiment. Resolved protein was transferred to a PVDF membrane (Biorad, #170–4273) with the Trans-Blot Turbo Transfer System (Biorad), blocked for 1 h at RT in incubated overnight in primary antibodies against RPS6$^{Ser235/236}$ (Cell Signaling Technology, 4858S), P-RPS6$^{Ser240/244}$ (Cell Signaling Technology, #5364S), P-4EBP1$^{Thr37/46}$ (Cell Signaling Technology, #2855S), P-4EBP1^{Thr70}(Cell Signaling Technology, #9455S), P-4EBP1^{Thr37} (Cell Signaling Technology, #9457S), P-Akt^{Ser473} (Cell Signaling Technology, #9271S), Akt (Cell Signaling Technology, #9272S), RHEB (Cell Signaling Technology, #13879S), RAPTOR (Sigma-Aldrich, #09–217), RPS6 (Cell Signaling Technology, #2217S), 4EBP1 (Cell Signaling Technology, #9644S), ß-actin (Cell Signaling Technology, #3700S), Rpl19 (Santa Cruz Biotechnology, sc-100830), Rpl7a (Cell Signaling Technology, #2415S), TXN (Aviva, ARP72618), AGR2 (Sigma, AV42290–100UL), SELENBP1 (Santa Cruz Biotechnology, sc-373726) and ANXA1 (Proteintech, #21990–1-AP) diluted to 1:1000 or PRDX1 (Cell Signaling Technology, #8499S) diluted to 1:500 in blocking buffer containing 5% bovine serum albumin (Sigma, A9647–100G) and 1xTBST (10mM Tris, 0.15M NaCl, 1% Tween), washed in TBST and incubated with Rabbit (GE Healthcare, GENA934–1ML) or Mouse IgG HRP Linked Whole Ab (GE Healthcare, GENA931–1ML) diluted to 1:10,000 in blocking buffer and incubated at RT for 1 h. Detection was performed on a ChemiDoc MP (Biorad) with Clarity Western ECL Substrate (Biorad, 170–5061) or SuperSignal™ West Femto Maximum Sensitivity Substrate (Thermo Fisher, 34095). In Figures 3, 5 and Extended Data Figures 5, 7-8 and 11, the corresponding ß-actin blots are shown directly below blots for target proteins. Because sequential antibody incubation and detection was performed to blot for multiple proteins, of distinct molecular weights, on the same membrane, the ß-actin blots may be shared between multiple blots and therefore are displayed multiple times for clarity. In Figures 3 and 5, lysates were harvested from at least n=3 axolotls per time point resolved on separate lanes. The green dashed line in Figure 3l illustrates the steady state protein expression based on the average (ß-actin normalized) level of a given protein in n=2 DMSO-treated animals at 0 hpa. In Figure 5a and Extended Data Figure 8a, each "mouse" lane represents a distinct pool of digit tips harvested at given time-point.

Co-immunoprecipitation

Wildtype or axmTOR expressing HEK293T cells were seeded on 10-cm^2 plates in standard growth media (10% FBS (Millipore, TMS-013-B) and 1x Penicillin-Streptomycin (Invitrogen, #5140163) in DMEM (Gibco, 11965–118)) so that they were ~80–90% confluent the next day (5.06×10^5 and 6.75×10^5 cells/mL respectively). Cells were briefly rinsed in 10mL/plate ice-cold 1xPBS (Gibco, #14190–250), incubated on ice for 5 min in 500–750 μL chilled lysis buffer (150 mM NaCl, 20 mM HEPES, pH 7.4 (ThermoFisher, 15630102), 2 mM EDTA, 0.3% CHAPS, cOmplete™, Mini, EDTA-free Protease Inhibitor

Cocktail (1 tablet per 10 mL, Sigma #11836170001) and 1x Halt™ Combined Protease and Phosphatase Inhibitor Cocktails Cocktail, EDTA-Free (ThermoFisher, #78443), scraped and transferred to tubes. Lysate was cleared by centrifugation at 13,000 rpm for 10 min at 4°C. Concentration of the cleared lysate was determined by Bradford assay following manufacturer's instructions (Biorad, #5000006) and for each sample 600 μg of protein was diluted in lysate buffer to a final concentration of 1 μg/μL. Of this volume, 50 μL was saved as an input sample and 500 μL were combined with 1 μL of mTOR antibody (Cell Signaling Technology, #2983S) in equal volume of lysis buffer and incubated overnight with head over tail rotation at 4°C. Next 25 μL/sample of Pierce™ Protein G Magnetic Beads (ThermoFisher, #88847) were washed in 175 μL of lysis buffer by gentle vortexing and separation on a magnetic stand. Beads were washed a second time in 1 mL of lysis buffer with gentle vortexing for 1 min. Then 500 μL of lysate with antibody was added to the pre-washed beads and incubated at room temperature for 1 h with rotation. Beads were collected on the magnetic stand and washed three times in 500 μL of lysis buffer and eluted in 2x Laemmli buffer (Fisher, #50–196-784) at 95°C for 10 min. Beads were magnetically separated from the lysate and lysate was transferred to a clean tube. Western blotting was performed as described above and membranes were incubated with antibody against RHEB (Cell Signaling Technology, #13879S) and mTOR (Cell Signaling Technology, #2983S) at 1:1000 dilution and detected with SuperSignal™ West Femto Maximum Sensitivity Substrate (Thermo Fisher, #34095) after incubation with HRP-conjugated secondary antibody (1:10,000, GE Healthcare, GENA934–1ML).

Drug administration studies

To assess the impact of mTOR inhibition on pathway activity (Figure 3g-k), translation (Figure 3l), accumulation of translationally upregulated proteins (Figure 3m-n) and wound closure (Figure 4a-b) and regeneration (Extended Data Figure 6h), we applied the same standard protocol whereby axolotls were anesthetized in Tricaine as described above. 100 mM (or 30.933 mg/mL) INK128 (LC Laboratories, I-3344) stock was prepared and stored at −80°C. Axolotls were anesthetized in Tricaine as described above, weighed and 125 mg of INK128 per 1kg of axolotl body mass, diluted in DMSO (or an equivalent volume of DMSO carrier control) in a total volume of 100 μL (topped up with 0.8x sterile PBS) were administered using an Insulin Syringe with a 28 1/2 G needle (Fisher Scientific, 114–826-205). After 4 h, the animals were anesthetized again and underwent amputation at 24 hpa or 48 hpa for western blot analysis or 12 hpa to assess translation on polysome gradients as described above. For tracking how administration of INK128 prior to amputation impacts the entire process of regeneration, the regenerating limb was briefly imaged under a light microscope at 1, 4, 7, 12, 21, 28, 35 and 42 dpa under anesthesia. Illustrations in Fig. 3e and Fig. 4j were made with Biorender.

To examine how mTOR inhibition impacts wound closure itself, we immersed white axolotl larvae (AGSC_101L35; 3–5 cm from snout to tail), in 10 μM INK128 dissolved in clean tank water (40% Holtfreter's Salt Solution). After 4 h, the axolotls were anesthetized and amputation was carried out as described above. After amputation, anesthetized larvae were immediately mounted in clean tank water containing anesthetic and underwent live imaging on the UltraVIEW spinning disc imaging set up describe above until 90 min post-

amputation. Representative videos of the process spanning from 30 minutes to 90 minutes post-amputation are included in Supplementary Videos 1-2. Percent wound closure for each animal was calculated by taking the difference of percent coverage of skin across the wound site at a starting time point (30 min post-amputation), and at 90 min post-amputation.

To examine the impact of Rapamycin on wound closure, axolotls were pre-treated with a high concentration of Rapamycin (10 μM, LC Chemicals, R-5000, n=3) dissolved in tank water (1 L of 40% Holtfreter's Salt solution) or DMSO (carrier, Sigma, D2650–5X5ML, n=3) for 14 h. Animals were anesthetized in Tricaine and the forelimb was amputated (as described in Methods). After amputation, the animals were placed in tanks containing fresh tank water (1 L of 40% Holtfreter's Salt solution) and a high concentration of Rapamycin (10 μM, n=2; 5 μM, n=1) or DMSO (carrier, n=3). Animals were imaged under anesthesia at 6 hpa (Extended Data Fig. 6a-c) and tissue was harvested for analysis by western blot (as described in Methods) (Extended Data Fig. 6d, Supplementary Data 1).

To assess role of mTOR beyond wound closure (Figure 4c), axolotls underwent the standard amputation protocol as described above. At 4 dpa, wound sites were examined for complete closure on all (12/12) animals and INK128 (or DMSO carrier control) was administered as described above at 125 mg of INK128 per 1 kg under anesthesia. INK128 or DMSO administration were repeated on the same animals at 6, 8 and 10 dpa, injections were administered on alternating sides. Animals were closely monitored and imaged under anesthesia on 4, 14, 28, 42 and 56 dpa. Chronic inhibition of mTORC1 was toxic and only 4/6 animals tolerated INK128 treatment for the duration of the study.

Administration of 4EGI-1 followed the same general procedure with the following details: in 4EGI-1^{low} experiments, we prepared 150 mM 4EGI-1 stock in DMSO. The animals were weighed and the stock was diluted in 0.8x PBS and 60 μL were administered by intraperitoneal injection at 125mg/kg body mass. Note that 4EGI-1 does not dissolve readily at higher concentrations, therefore for 4EGI-1high experiments 10 μL of drug (150 mM 4EGI-1 in DMSO) was combined with 30 μL PEG3000, and diluted in a final volume of 61 μL 0.8x PBS brought to neutral pH with sodium hydroxide. Animals were weighed and injections were administered bilaterally for an effective dosage of 260–290mg/kg. Next, 3.5 h after amputation, animals were anesthetized and forelimb amputations were performed as described above. Images were taken at 24 hpa to assess wound closure.

To administer V-9302, a 185 mM stock solution was prepared in sterile water, animals were weighed and 60 μL of drug dissolved in 0.8x PBS was administered by intraperitoneal injection at a final dosage of 126 mg/kg. The animals were anesthetized 3.5 h after injection and amputation was performed as described above. Animals were imaged at 24 hpa to assess wound closure.

To examine whether inhibition of mTOR signaling impacts ROS accumulation after amputation, white axolotl larvae (AGSC_101L35; 3–5cm snout to tail) were immersed in 10 μM INK128, or DMSO control, for 4 h and underwent amputation as described above. The larvae were housed in 10 μM INK128 (or DMSO) containing water and at 36 hpa they were treated with 5 μM 2',7'-dichlorodihydrofluorescein diacetate (H_2DCFDA)

(Biotium, #10058) for 55 min, and immediately mounted in clean tank water containing anesthetic and imaged. We examined n=5 INK128-treated larvae and n=4 DMSO-treated controls. Single-plane brightfield and H$_2$DCFDA fluorescence images of cells lining the wound site of the animal were acquired at a mid-point in the tissue. For quantification, cell boundaries for each image were manually traced in the bright field channel, and then the mean fluorescence intensity of H$_2$DCFDA was quantified for each defined cell using ImageJ. The layer of tissue with defined cells is outlined on representative images in Figure 4e.

For treatment with Apocynin (APO, Santa Cruz Biotechnology), white axolotl larvae (AGSC_101L35; 3–5cm snout to tail) were immersed in 400 μM APO (n=3) dissolved in 40% Holtfreter's salt solution or a comparable concentration of DMSO (control, n=3) for 1 h prior to amputation. The axolotls were then raised for 3 days in 400 μM Apocynin or DMSO. The treatment solution was changed daily. On day 4, the animals were transferred to untreated Holtfreter's for the remainder of the experiment. The animals were imaged at 2, 3, 7 and 19 dpa. There were no phenotypic differences between groups prior to 7 dpa. At 7 dpa, the area between the skin layer covering the blastema and the tips of the bones was compared to the total limb area to the region of hypertrophic chondrocytes and was expressed as a percentage area. Areas were quantified using ImageJ, and significance value was evaluated using a two-tailed Student's t-test. P-value < 0.05 was deemed significant.

Multiple Sequence Alignment

To screen for axolotl-specific changes in the mTORC1 pathway, the protein sequences for human mTORC1 pathway components were retrieved from Uniprot and their orthologues were identified in chimp, macaque, mouse, xenopus and zebrafish by protein-to-protein BLAST (https://blast.ncbi.nlm.nih.gov/Blast.cgi). Next, axolotl mTORC1 pathway components were retrieved from https://www.axolotl-omics.org/blast by performing a tblast search against the human sequence. The percentage of amino acid identity between axolotl, human and mouse sequences is reported in Supplementary Data 5. A multiple sequence alignment was performed using Uniprot's 'Align' feature using default settings. The alignment was inspected to identify regions with divergent sequences unique to axolotls. This identified insert 1 and insert 2 within axolotl mTOR as regions of interest. To confirm the presence of these inserts across amphibians, which are generally poorly annotated, we searched for mTOR orthologues in the Transcriptome Shotgun Assembly Sequence database. Analysis of the insertion region confirmed that insert 2 was present exclusively within urodele amphibians whereas insert 1 was more broadly conserved across amphibian species. The presence of the insert was further confirmed by examining the sequence reads in our libraries and by amplification by RT-PCR. To conduct a more comprehensive multiple sequence analysis, we retrieved full length mTOR mRNA, and where available protein, sequences for a representative subset of amphibian and non-amphibian species. The mRNA sequences were *in silico* translated with the ExPASy Translate tool and used for multiple sequence alignment using the Uniprot align feature and rendered using the Espript version 3.0 (https://espript.ibcp.fr/ESPript/ESPript/) and the full alignment is shown in Supplementary Data 6-7. The insert region from a comprehensive multiple sequence alignment of sequences from 97 unique mammals, 28 ray-finned fish, 1 lobe-finned fish, 1

cartilaginous fish, 1 lungfish, 37 species of birds, 1 crocodilian, 6 turtles and tortoises, 12 snakes and lizards, 4 caecilians, 15 frogs and toads, and 9 newts and salamanders performed in Clustal Omega is included in Supplementary Data 7.

Structure modeling

The predicted model of axolotl mTOR insertion (residues 951–1122) was generated using the transform-restrained Rosetta (trRosetta) algorithm, a deep learning-based protein structure prediction method[63]. All figures were generated using Pymol. A model of the axolotl mTOR insertions was built using the transform-restrained Rosetta (trRosetta) algorithm and superimposed on RHEB-bound mTORC1 dimer (PDB 6BCU). Intriguingly, both insertions reside on mTOR dimerization or effector binding interface, suggesting a potential functional impact on axolotl mTOR. The first insertion (insert 1) in axolotl mTOR contains seven more amino acids (residues 1001–1007) than human mTOR near one of the RHEB switch II region interacting segments. This extended RHEB binding surface in axolotl mTOR might modulate how RHEB allosterically activates the kinase domain. The second insertion (insert 2, residues 1039–1058) in axolotl mTOR is located at the dimerization interface. The predicted model of two insertion 2 suggests a neo-interaction between two axolotl mTOR molecules.

Generation of chimeric human-axolotl mTOR kinase in HEK293T cells

To model the impact of axolotl specific inserts of the function of mTOR kinase, we used Clustered Regularly Interspaced Short Palindromic Repeats (CRISPR) with CRISPR-associated protein 9 (Cas9) to scarlessly insert these insertions into the human genomic locus encoding mTOR in HEK293T cells (kind gift from J. Frydman) which are an established model to study mTOR function[36,64]. To do this we designed donor templates encoding a human exon 20 carrying an in-frame axolotl insert 1 and a separate donor template encoding a human exon 21 and an in-frame axolotl insert 2. The insertion region was flanked by homology arms ~300 bp in length (for details see Extended Data Figure 9a). Two guide RNAs (gRNAs) were selected within introns flanking each desired site of insertion and ordered as oligos (IDT). The sequences are listed below. The protospacer adjacent motif (PAM) sequence of each gRNA sites was mutated in the donor templates to prevent re-cutting of the repaired genomic DNA. Note that in all cases the gRNA sequence was intronic. In addition, copies of the gRNA and PAM sequence were appended to the 5' and 3' ends of the donor template to enable excision of the donor template from a plasmid as a linear double-stranded DNA "double-cut donor" and increase efficiency of homology-directed repair[65]. A 997 bp donor template containing insert 1 and a 1,363 bp donor template containing insert 2 were synthesized by CODEX DNA (https://codexdna.com/), subcloned into a TOPO cloning vector with a Zero Blunt™ TOPO™ PCR Cloning Kit for Sequencing (Invitrogen, #450031). The gRNAs were subcloned into a PX459 vector (addgene #62988)[66] and sequenced to confirm correct insertion. HEK293T cells were seeded in a 6-well plate so that they were 70–90% confluent the next day (~0.8×10^6 – 1×10^6 cells/well in 2 mL of standard growth media containing 10% FBS (Millipore, TMS-013-B) and 1x Penicillin-Streptomycin (Invitrogen, #5140163) in DMEM (Gibco, 11965–118)). Next day, fresh media was added and after 30 min the cells were transfected with CRISPR reagents for insert 2 insertion using the Lipofectamine 3000 Transfection Kit

(Invitrogen, L3000001) per manufacturer's instructions. We used 1600 ng donor template (in TOPO), 400 ng each of 5' and 3' gRNA in PX459 vector, 4.8 μL of P3000 reagent and 3.57 μL of Lipofectamine 3000 in a total volume of 250 μL of Opti-MEM(Invitrogen, 31985070). The next day, the cells were split to a 10 cm plate. Puromycin selection was initiated the following day with 1 μg/mL of puromycin dihydrochloride (Sigma P8833–10MG). Puromycin in fresh growth media was added after 24 h. After 48 h of selection, 1/2 of the cells were frozen down, 1/4 were used to extract DNA for PCR verification of insertion within the cell pool and the remaining 1/4 of cells were split to a new 10 cm plate. The following day individual selected cells were trypsinized in 0.05% Tryspin-EDTA for 5min at 37°C, pelleted by centrifugation at 1,000 rpm for 4 min and resuspended in sorting buffer containing HBSS (Gibco, #14175–079), 2% FBS, and 1mM EDTA and filtered. Individual live cells were sorted on into wells of a 96-well plate containing fresh growth media. At least 3 plates were prepared for each construct. After 1 week the growth media was changed once per week and clones reached confluency after two weeks. Clones were screened for insertion by PCR. Homozygous insertion was confirmed by sequencing. After clone containing homozygous insertions of insert 2 were successfully expanded, the above protocol was repeated to introduce homozygous insertion of insert 1. Two independent clones doubly homozygous for insert 1 and insert 2 were generated and used for downstream analysis.

Oligo sequences for gRNAs were as follows for insert 1:

gRNA_ 47163 caccGTCTCAGTAGATAGTGTAGTG & CAGAGTCATCTATCACATCACcaaa, gRNA_47478caccGAGCTGTTACAGTCTTAGTAC & CTCGACAATGTCAGAATCATGcaaa

Oligo sequences for gRNAs were as follows for insert 2:

gRNA_49826 caccGGGGGGAGTGAGGAGTTGATCT & CCCCCTCACTCCTCAACTAGAcaaa, gRNA_50114 caccGAAATC AGAAAATCTCTCTGG & CTTTAGTCTTTTAGAGAGACCcaaa

>insert1_donor_template

CCTGTACTAAGACTGTAACAGCTTAAGAGACAGGGTCTCACCCTGTCACCCTGCA
CTCTGT
AGAGTGCAGTGGCACGTGCATAGCTCACTACAGCCTTGAACTTCTGGGCTCAAGC
ATTTCT
CCCACCTTAGCATCCAGTAGCTAGAACTACAGGCAAGTGCCCAGCTAATTTTTTGT
ATTTTT
TTTGTAGAGACAGGATCTCGCCATGTTGCCCAGGCTGTTCTTGAAATCTTGGCCTC
AAGCA
GTCCTCCCGCCTTGGCCTCCCAAAGCACTGAGCCTCCAAACCTAGCCAAGCTTGG
GTCTT
TGAAATATATTCTCAGTAGATAGTGTAGTGTGCAAACCCATTCCATAGTTGCCTTTA
TTTGTT
CACATGAGCTTAAGGTAAGCCTGGGGGTTCAATGTCCTTCATGATACCAGCTGGTT

GACCT

CTTGTCCATTTCAGTCCCACCAGCCTTCTCCCCAATTCATGTTCCAACAGCTGGGG
ATGCT

AGTGTCCTTTGTACGGAGTCACATCCGGCCGTACATGGAGGAAATATTCTCTCTCA
TGAGA

GTGAGTAGAAGTTAATGCTTTGGCCTCTTCCATGTTTGGGTCAAGGAAGGCTCAG
AAGCAA

GTTTGAATGACATAGACTTTTTTTCACGGATCTTTGTAGAGCTGTTACAGTCTTAGT
ACAGC

AAGTGGAACAAAGCCCACTGGATTTTGAGGGGGAGGAAGGGCTGTTGCTCCAGG
TTCCA

GGTACAAAACTACAAGGCATGAAGGCTGAAGAGAAATCCTGCAGTAATTGTTCTG
CCAGAA

ATAGACAATTGGGTTATTTGCCTCACACACAACAAAGCAATTTTACTTTAATATCAC
AAGGG

TGCTTTTCTATTTTCATGAAAGCCCTCTTTGTTACTGCTCATAAACCATGAAGGGAT
TGGGT

TTTCTTAGGGCTGTTAAATATGATGGACACGTGTTGGGCACCAAGGAACAAGGTG
CCACAC TACACTATCTACTGAGA

>insert2_donor_template

GCGTTTAAACGAATTCGCCCTTAAATCAGAAAATCTCTCTGGAGGGTCTAGAGGG
AGGACA

GCAAAGCAAAGGAAGTCTTACAACTGCTATCGCTATCAAAGGGAGTGCAAAGGA
CCCAAGT

GGATCATGGAAGGAGAAGAAGAAAGCCTGCATGGGAGAAGTGAGGCTAGAGCCA
GGTCT

AGAAAGACAGACAGGGCTTAGCTGAGCAAGAAGTGGGATTCTAGGCAGAGGAAG
CAGCAT

GAGCAAAGCCCAGAGGACTGAGGTAGCCTGGTGCATCTGGGGAAATGCAATTGA
GTTTGT

CCAGTGTAGCTGCAACATAGGACACAAGAAGGGCCCAGTGGGAGGAGGGGAGTG
AGGAG

TTGATCTCGCCGCAGACCATGCTCACTACAGTTTTGCTTTTCTGGCCATCTTGATTC
CTTTG

TTCATATATCATCAGAAAGGGACCTGACTCAGCTCCTCTGACTTTTCTCTCTTTGTA
GGAAT

TGAAAACGGATGTCTTGGAGACAACAGATCCATTGAGGACAGACTCAAATAAGGA
TCACTG

GACAACGAATAACCCAATTCAGAGCACGATCATTCTTCTCATTGAGCAAATTGTGG
TAGCTC

TTGGGGGTGAATTTAAGCTCTACCTGCCCCAGCTGATCCCACACATGCTGCGTGTC
TTCAT

GCATGACAACAGCCCAGGCCGCATTGTCTCTATCAAGGTGAGTAGCCTACGTCATC
TTCCA

GAGAGATTTTCTGATTTCCTCTGAGTCCCTGGGTGATCAGCTAAAAGCTGAGACCT
CATTC
TGAGTGACAGGTTGATGCCCATTCCATAAGACAGAATCCCAAGAATACTAATACCC
AATGT
GTGCAGTTTACAGAATGTCTGTAATCCTCTCTTGATTATCCTTATGTTTTGTATCTGT
TTCAA
TGGATTAATCTTGGGAAATATTTTATCCCAGACTAATTTTCTTTATTTTCCAGCAAC
GGATTC
CTTATCAACTCAAATAAGCACAGAGAAAGCAAAGTAATATGTAAGCAAATAAAAT
GAGGGGA
AGAAAGTGCTATCAAAAGGATATAGTTCAAGGCCATTTAATAAAGAGTTTTCCCAG
TCCCCA
GAGAACTTTGAATTGTCTACACCACCACCCGCTGCGTGTCCTTAGCCGAGATCAA
CTCCTC ACTCCCCAAGGGCGAATTCGCGGCCGC

Characterizing the function of chimeric axmTOR

To characterize the impact of axolotl inserts on the function of mTOR kinase, we subjected the chimeric HEK293TaxmTOR cells and wildtype controls (both the untreated parental HEK293T line and a line that underwent the CRISPR/Cas9 protocol described above but maintained the wildtype sequence). To assess the nutrient sensitivity of the chimeric mTOR, Wildtype or chimeric HEK293T cells were seeded in 12-well plates at 250,000 to 275,000 cells/mL in standard growth medium (10% FBS, 1x penicillin/streptomycin, DMEM). The next day, the cells were rinsed once in RPMI without amino acids, glucose or serum (US Biological, R9010–01) to remove traces of growth media and starved in RPMI supplemented with 10% dialyzed FBS (Invitrogen, A3382001) and 1x glucose (Invitrogen, A2494001) for 50 min. Next, we prepared a 2-fold dilution series of a 1x "stimulation" solution containing 1x essential amino acids (Invitrogen, 11130051), 1x non-essential amino acids (Invitrogen, 11140050), 1x L-glutamine (Sigma, TMS-002-C), 10% dilayzed FBS and 1x glucose in RPMI. Wildtype or chimeric HEK293T cells were re-fed with 1 mL of "stimulation" solution, ranging in concentration from 1x to 0x, for 30 min. After 30 min, the cells were rinsed with 1x PBS and lysed by incubation with RIPA buffer on ice for 20 min. The cells were then cleared, sonicated and underwent quantitation with BCA and western blotting against phosphorylated and total RPS6 and 4EBP1 as described above in the "Western blotting" section. Three independent titration experiments were performed on the parental HEK293T line and chimeric clone C1, a representative blot from one experiment is shown in Figure 5 and Extended Data Figure 10 (for replicates see Supplementary Data 1).

To assess the capacity of the chimeric mTOR to sense nutrient starvation and stimulation over time, we seeded cells as described above and starved them for 30 min, 50 min, or 80 min by incubating them in RPMI (US Biological, R9010–01) without amino acids, glucose or serum. Cells were rinsed in 1xPBS and harvested in RIPA buffer at these time-points. After 50 min (the standard starvation interval described in previous work), a subset of starved cells was stimulated by addition of 1x amino acids (essential, non-essential and L-glutamine), 1x glucose and 10% dialyzed FBS. Cells were rinsed with 1xPBS and harvested by lysis in RIPA buffer after 5 min, 10 min, 20 min and 30 min of stimulation. The

cells underwent clearing, sonication, BCA quantitation and western blotting against total and phosphorylated RPS6 and 4EBP1 as described above. The data shown represent two independent experiments performed on two independent chimeric and wildtype clones of HEK293T cells. Graphs were plotted in GraphPad Prism 9 and Student's t-test was used to determine significance.

Lastly, to examine the impact of insertions on lysosomal localization, 200,000 wildtype or chimeric cells were seeded onto fibronectin-coated glass coverslips (Millipore-Sigma, F1141–1MG) in 6-well plates. The next day, each well was gently rinsed once with RPMI and then starved for 50 min in 2 mL of RPMI (without amino acids, glucose or FBS) with 20 μM Lysotracker Red DND-99 (Invitrogen, L7528). After 50 min of starvation, the cells were stimulated by addition of 1x essential amino acids, 1x non-essential amino acids, 1x L-glutamine, 1x glucose, and 10% dialyzed FBS directly to the medium and incubated for 10 min. For control cells, the Lysotracker was added directly to the existing media. The cells were then rinsed with 2 mL of 1xPBS containing Lysotracker and fixed in 4% paraformaldehyde in PBS for 15 min at RT. After incubation the cells were rinsed twice with 1xPBS and permeabilized for 10 min at RT with 0.1% saponin. They were rinsed with 1x PBS again and incubated with 50 μL of blocking solution (1x PBS, 0.5% goat serum) with 1:300 anti-rabbit mTOR (Cell Signaling Technology, #2983S) for 1 h at RT. The cells were washed three times with 1xPBS and incubated with 1:1000 Alexa 488 secondary antibody (Invitrogen, A11070) and 1:1000 DAPI for 45 min at RT in the dark. The cells were rinsed three times in 1xPBS and mounted on slides using Fluoromount-G Slide Mounting Medium (Southern Biotech, 0100–01). Slides were images on a Zeiss Axio Observer Z1 microscope coupled to the Perkin Elmer UltraVIEW Vox spinning disk confocal microscopy system. Analysis was performed using custom code written in Python 3.7. The mean fluorescence intensity of mTOR (488 nm laser channel) was measured within lysosomes defined by Lysotracker (568 nm laser channel) using local adaptive thresholding in individual cells defined by manually outlined cell boundaries. Cell boundaries were carefully drawn in Fiji/ImageJ based on DAP (405 laser channel) and mTOR staining. For each cell line and condition, the lysosomal intensity is expressed relative to the mean steady state intensity for that specific cell line. Significance assessed with one-way ANOVA calculated in GraphPad Prism 9. The experiment was performed three independent times.

Cell Viability Assay

Wildtype HEK293T cells or HEK293T[axmTOR] sells were seeded at a density of 100,000 cells/mL on 96-well plates, allowed to attach at least 12 h and treated with INK128 (Selleckchem, #S2811) at indicated concentrations for 48 h in standard growth media. A CellTiter-Glo Cell Viability Assay (Promega, G9241) was performed following the manufacturer's instructions and absorbance was measured at 490nm using a GloMax-Multi Plate Reader (Promega, E6521). Three independent experiments were performed. The IC50 values for each replicate was calculated in Prism 9 by performing nonlinear regression for inhibitor vs response (variable slope-four parameters). The average of three IC50 values +/− standard deviation is shown in Figure 5l. Significance was calculated using Student's t-test.

Polysome Profiling by qPCR

Wildtype and HEK293T^{axmTOR} cells were cultured on 10-cm^2 plates. Once the cells reached 80% confluency, they were washed in 1x PBS and RPMI starvation media free of amino acids, glucose or FBS was added for 50 min as described above. The cells were re-fed by addition of 1x essential and non-essential amino acids, L-gln, FBS and glucose as described above. After 6 h of growth, the cells were treated with 100 μg/mL cycloheximide (Sigma) for 2min, scraped and washed with ice-cold 1x PBS containing 100 μg/mL cycloheximide. Cells were lysed using polysome buffer containing 10mM Tris-HCl (pH 8.0), 150mM NaCl, 1.5mM MgCl2, 0.25% NP-40, 0.1% Triton X-100, 50mM DTT, 150 mg/mL cycloheximide, and 640U/mL RnaseOut Ribonuclease Inhibitor (Promega, N251A) on ice for 30 min. Lysates were cleared by centrifugation at 10,000 g for 10min at 4°C. The supernatants were adjusted by OD260 concentration and loaded onto a 10%–50% sucrose gradient before centrifugation at 37,500 rpm for 2.5 hr at 4°C in a Beckman L8–70M ultracentrifuge. Samples were separated on a Biocomp fractionation system to evaluate polysome profiles and collect polysome fractions. 14 fractions were collected for each sample in total and RNA was isolated from each fraction, except the first two. Next, 750μL of Trizol LS (Invitrogen, #10296010) and 0.4 μL of 1 mg/mL glycogen (Roche, #10901393001), together with 10ng *in vitro* transcribed Firefly Luciferase (FLuc) spike mRNA, were added to 250 mL of sucrose lysate and incubated for 15 min at room temperature. 200 μL of chloroform was added to the mix before spinning down the samples for 15 min at 12,000 g at 4°C. RNA was precipitated by adding 500 μL of isopropanol to the supernatant overnight at −80°C. The next day the samples were spun down for 20 min at 16,000 g at 4°C. The pellet obtained was washed with 70% ethanol and resuspended in dH$_2$O. Any trace DNA was removed with the Invitrogen TurboDNA-free kit (Invitrogen, AM1907). cDNA was synthesized using the same volume of RNA as template from each fraction. High-capacity cDNA reverse transcription kit was used (Applied Biosystem, #436884) following the manufacturer's protocol. qPCR analysis was performed using PowerUp Sybr Green master mix (Applied Biosystem, #A25917) on QuantStudio 6 Flex (Applied Biosystem). Fluc mRNA is used as an internal control to normalize each fraction.

Primers used for polysome qPCR:

DK2065	HsRpl19-qPCR-F1	CGAGCGAGCTCTTTCCTTTCG
DK2066	HsRpl19-qPCR-R1	AGGCTGTGATACATGTGGCG
DK2067	HsRpl7a-qPCR-F1	ATAAGCGGCTGAAAGTGCCT
DK2068	HsRpl7a-qPCR-R1	ACGGTGTTAACTCCTGCTCG
DK2093	HsCIRBP-qPCR-F1	CCCGACTCAGTGGCCG
DK2094	HsCIRBP-qPCR-R1	CGGATCTGCCGTCCATCTAC
DK260	HsActin qPCR-F	GCAAAGACCTGTACGCCAAC
DK261	HsActin qPCR-R	AGTACTTGCGCTCAGGAGGA
DK272	Fluc-qPCR-F	CAACTGCATAAGGCTATGAAGAGA
DK273	Fluc-qPCR-R	ATTTGTATTCAGCCCATATCGTTT

Extended Data
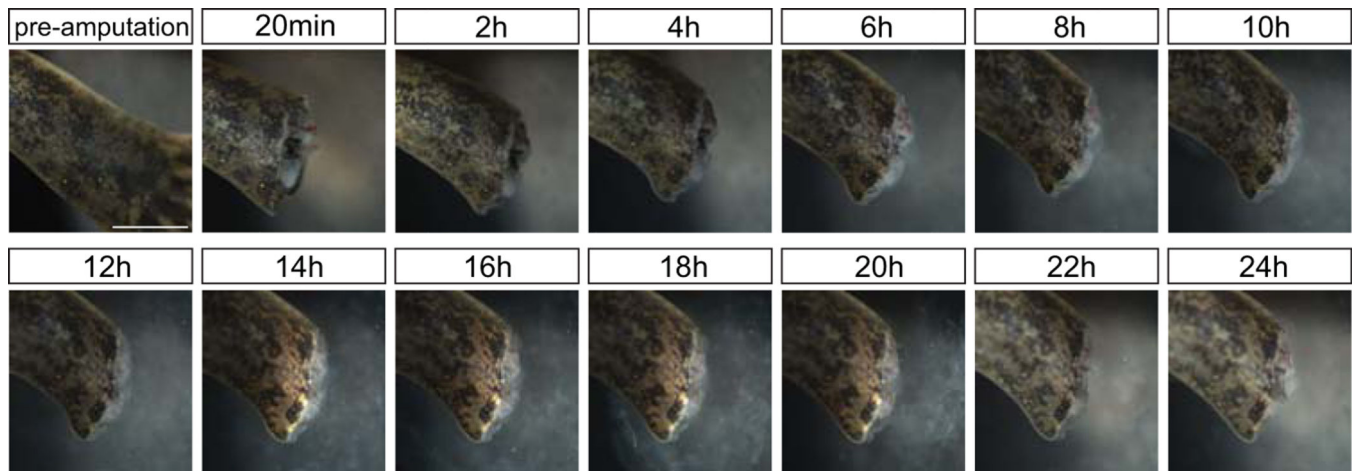
Extended Data Figure 1: Rapid epithelial migration drives wound closure.
Snapshots of wound closure in a wildtype sub-adult axolotl imaged over the course of 24 h.

Scale bar is 200 px (~0.90 mm).
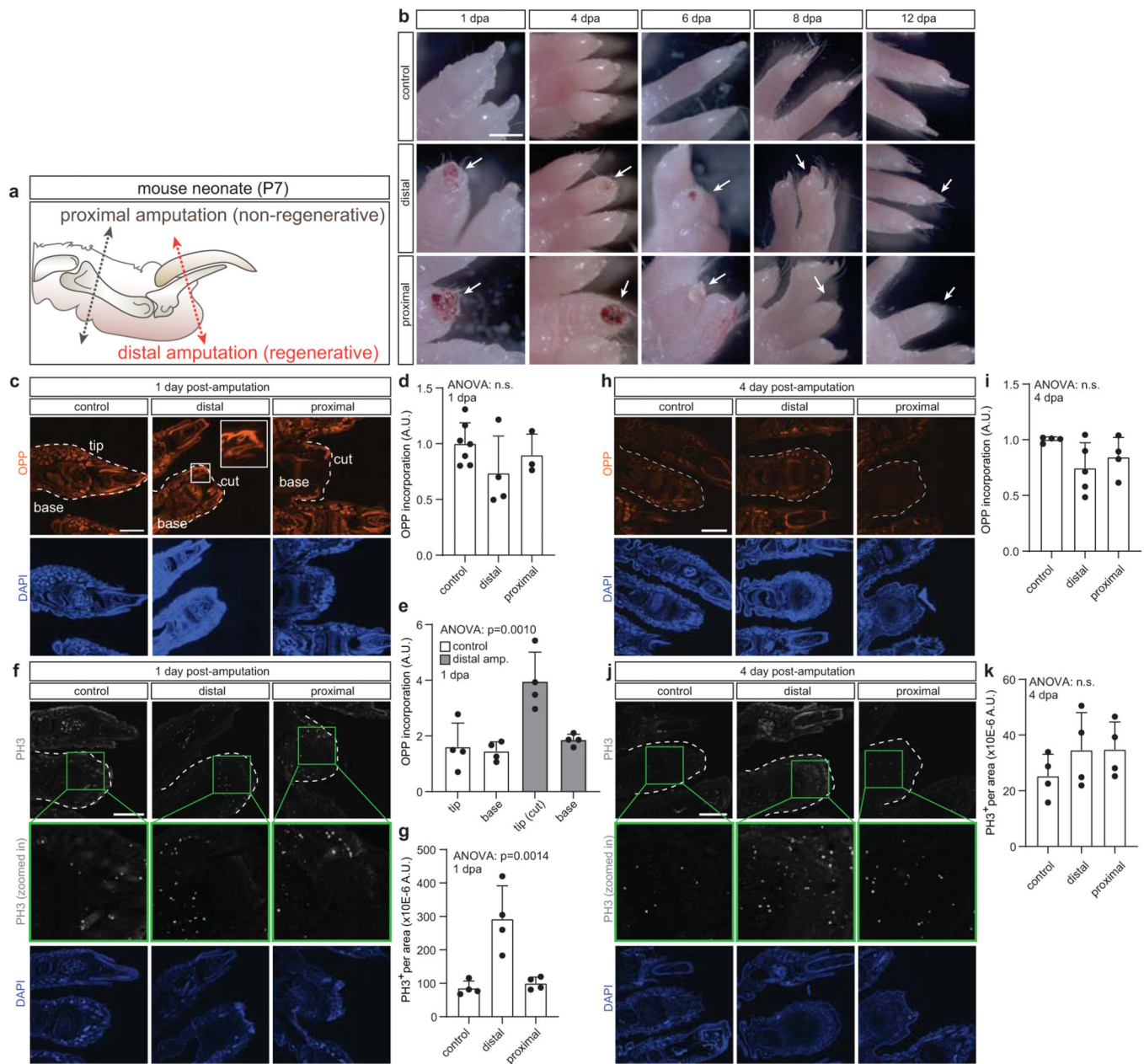
Extended Data Figure 2: Protein synthesis and proliferation in the mouse digit.
a, Schematic depicts location of proximal (black arrow) or distal amputation (red arrow). **b**, Representative images of mouse digits at 1, 4, 6, 8 and 12 days after amputation (at least 3 animals were imaged for each treatment and time-point). **c**, OPP incorporation in mice after distal and proximal amputation at 1 dpa. Inset illustrates elevated OPP incorporation at the cut site. Dashed line outlines digit of interest (doi). **d**, Quantitation of OPP signal in the doi shows no significant changes between controls (n=7), proximal (n=3) or distal amputations (n=4) at 1 dpa. **e**, Quantitation shows elevated OPP signal in skin near the cut site after distal amputation (signal at cut site is compared to signal at base of digit for control (n=4 individual mice) or distal amputations (n=4 individual mice), both normalized to total OPP across digit). **f**, PH3 incorporation assessed at 1 dpa. **g**, Quantitation of PH3^{+}

cells per tissue area (n=4 individual mice per treatment) reveals increased proliferation after distal amputation. **h**, OPP incorporation assay at 4 dpa. **i**, Quantitation of OPP incorporation across the digit (dashed line) for n=4 control, n=5 distal and n=4 proximal amputations from individual mice. **j**, PH3 incorporation assessed at 4 dpa. **k**, Quantitation of PH3+ cells per tissue area for control, distal and proximal amputations at 4 dpa in n=4 individual mice per treatment. Statistical analysis was performed with one-way ANOVA. P values > 0.05 were considered not significant and are denoted by n.s. Mean ± s.d. are shown in all plots. Scale bar is 1 mm in 2**b**; 500 μm in 2**c**, **f**, **h** and **j**. In **a-j**, 1 digit was amputated per mouse and each n is an independent animal.
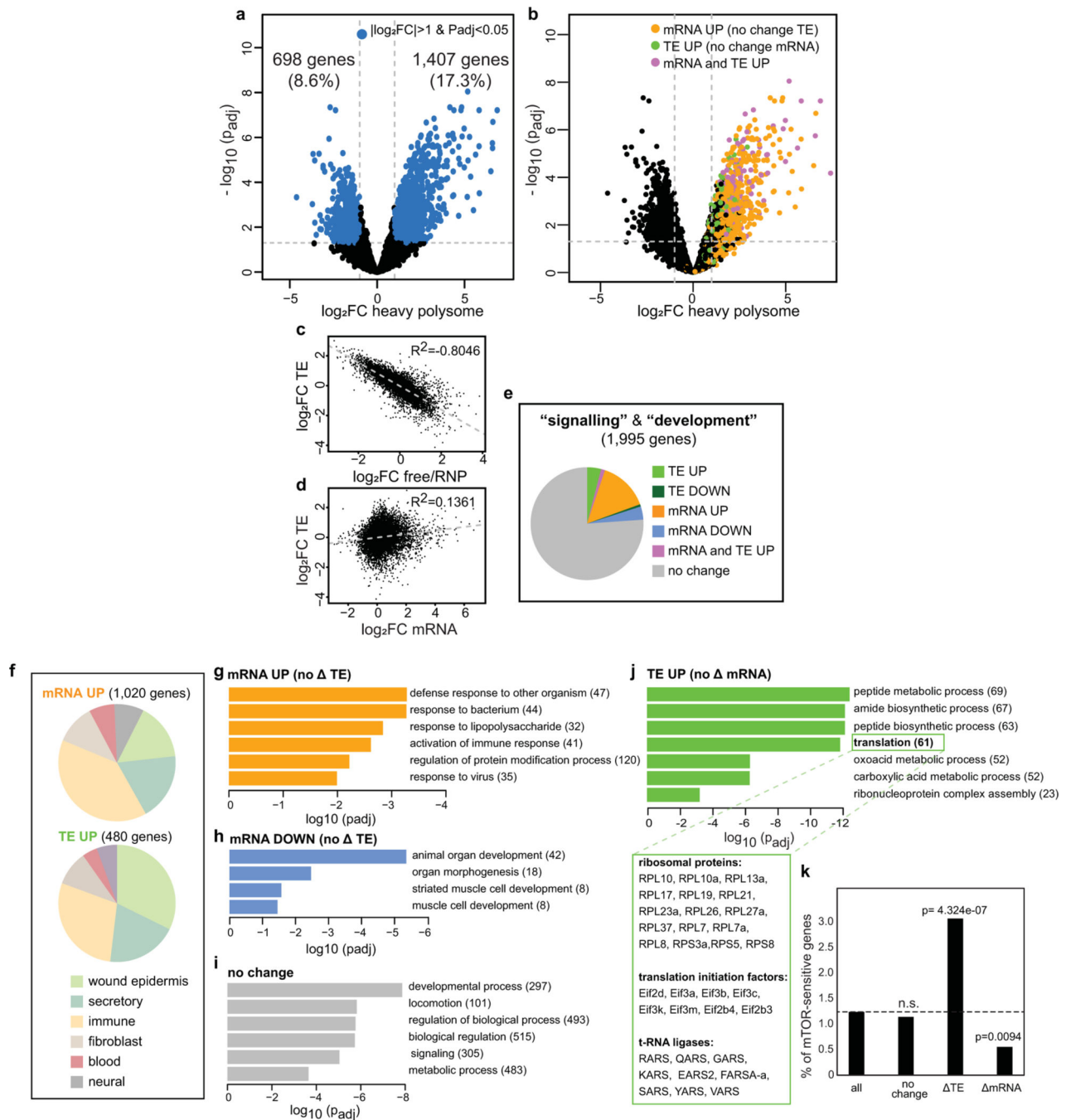
Extended Data Figure 3: Polysome sequencing identifies translationally regulated mRNAs
a, Scatterplot of 8,139 transcripts in our data set. The x-axis shows ($\log_2$) fold change (FC) in the heavy polysome fractions between 0 h and 24 h post-amputation. Y-axis shows (-$\log_{10}$) p-values (p_{adj}) adjusted for multiple-testing using the Benjamini-Hochberg method. Blue dots indicate transcripts with $p_{adj} < 0.05$ and two-fold change in the heavy polysome. **b**, The scatterplot from panel (a) colored to emphasize that transcripts with increased reads in heavy polysome include transcripts that are upregulated at the level of transcription (orange), translation (green) or both (pink) as defined in Figure 2b, therefore

change in heavy polysome on its own does not adequately describe the provenance of actively translated transcripts. As in b, p-values (p_{adj}) were adjusted for multiple-testing using the Benjamini-Hochberg method. **c**, Strong negative correlation between ($\log_2$) FC in TE on y-axis and ($\log_2$) FC in the free/RNP fraction. **d**, Poor correlation between ($\log_2$) FC in TE on y-axis and ($\log_2$) FC in mRNA abundance between 0 h and 24 h shown on x-axis. **e**, Distribution of 1,995 genes with annotated roles in "signaling" and "development" across expression categories defined in Figure 2b. **f**, Overlay of our data with previously published single-cell RNA-Seq analysis[10] suggests that translationally regulated mRNAs (green in Fig. 2b) are enriched in the skin. **g**, Gene Ontology (GO) enrichment analysis of transcript subsets defined in (Fig. 2b) reveals enrichment of immune processes in the orange category, **h**, enrichment of cell differentiation genes in the blue category, **i**, enrichment of developmental processes and signaling genes in the grey category, **j**, enrichment of translation and metabolic processes in the translationally activated (green) category. Box shows subset of transcripts enriched in the "translation" GO category. For **g-j**, the adjusted p-values were determined using the Benjamini and Hochberg method. **k**, Distribution of orthologues of established TOP/PRTE-containing mTOR-sensitive genes in our data set shows significant enrichment within translationally regulated gene set based on a two-sided binomial test, n.s. is p > 0.05 and is not statistically significant; exact p-values are shown for comparison of TE, mRNA and "no change" categories to "all".
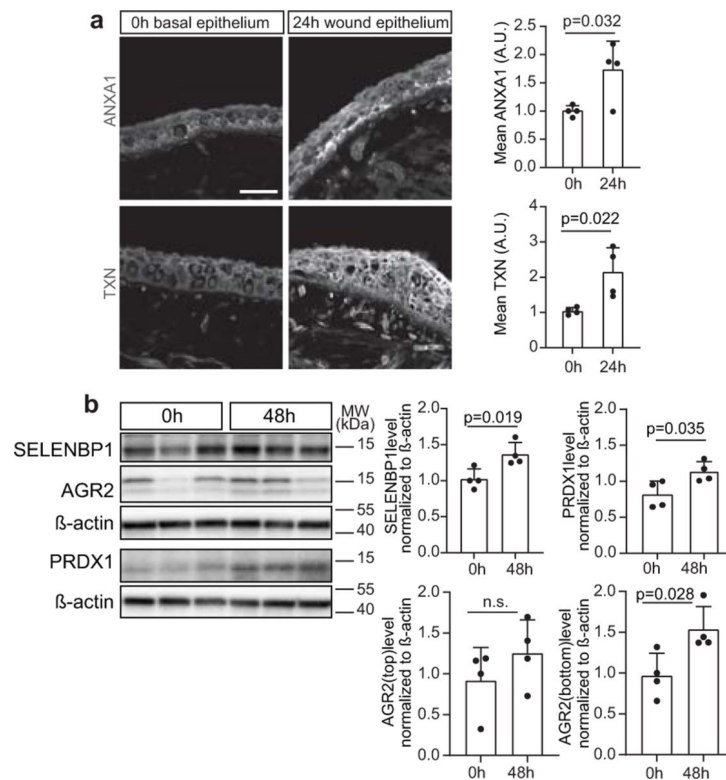
Extended Data Figure 4: Elevated expression of translationally activated targets.
a, Immunofluorescent staining of tissue sections highlights increased expression of translational targets ANXA1 and TXN in the axolotl basal epithelium at 0 hpa and wound epithelium (WE) at 24 hpa (n=4 individual axolotls per time-point). Scale bar is 100 μm. **b**,

Western blot of tissue harvested from the plane of amputation shows increased expression of translational targets SELENBP1, AGR and PRDX1 at 48 hpa (tissue harvested from n=4 individual axolotls per time-point and processed independently). Student's t-test, two-tailed, was used to assess significance in adjacent graphs, n.s. indicates p > 0.05 and deemed not significant. Mean ± s.d. shown in all plots.
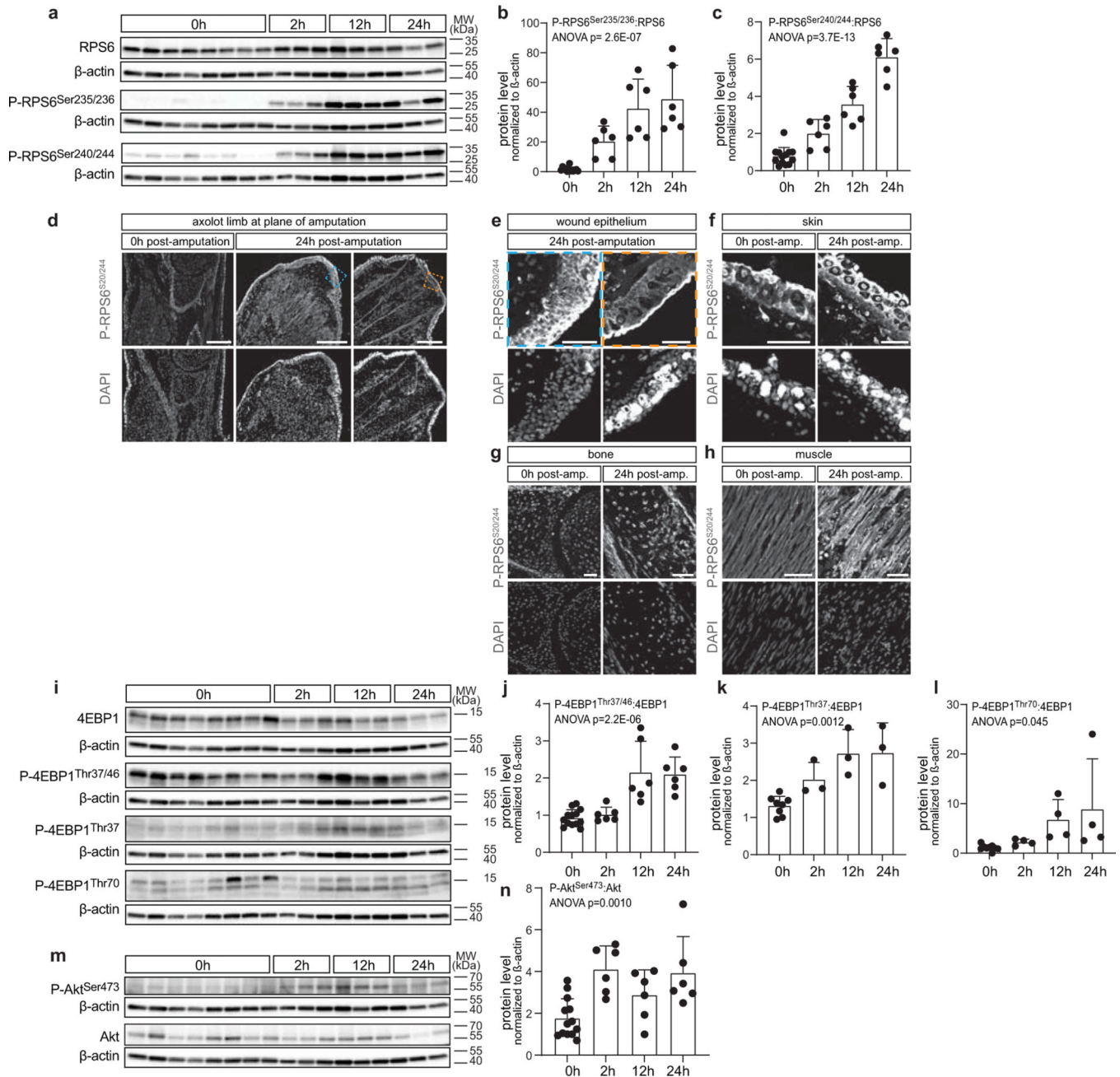
**Extended Data Figure 5: Rapid activation of mTOR signaling after amputation.**
a, Limb tissue lysates were harvested at indicated time-points after amputation. Each lane contains tissue from an individual animal assessed by western blot for changes in mTOR activity with antibodies against total and phosphorylated RPS6. **b**, Quantitation of

P-RPS6$^{Ser235/236}$ and **c,** quantitation of P-RPS6$^{Ser240/244}$ each normalized to total RPS6 and ß-actin. **d,** Immunofluorescent staining of P-RPS6$^{Ser240/244}$ is elevated throughout limb and particularly in WE at 24 hpa shown in tiled images of whole limb (blue and orange boxes show region of WE enlarged in panel e). **e,** in the wound epithelium, **f,** skin, **g,** bone, **h,** muscle. Images in **d-h** are representative of tissue staining from n=3 individual axolotls. **i,** Western blot of total and phosphorylated 4EBP1. **j,** Quantitation of P-4EBP1$^{Thr37/46}$, **k,** P-4EBP1^{Thr37} and **l,** P-4EBP1^{Thr70}, each normalized to total 4EBP1 and ß-actin. **m,** Western blot and **n,** quantitation of P-AktSer^{473} normalized to Akt and ß-actin. In **b-c, j-l, n,** statistical significance was assessed with one-way ANOVA for cumulative data from western blots shown here in **a, i, m** and in Fig. 3a-b. Complete raw blots are in Supplementary Data 1. A p value < 0.05 was deemed significant. Mean ± s.d. shown in all plots. In b-c, j, and n above we examined tissues from n=13 individual axolotls at 0 h and tissues from n=6 individual axolotls per time-point at 2 h, 12 h, and 24 (18 axolotls in total). In k-l above, we examined tissues from n=8 individual axolotls at 0 h and tissues from n=3 axolotls per time-point at 2 h, 12 h and 24 h. Scale bars are all 500 μm in 5**d**; 100 μm in 5**e, g,** and **h.**
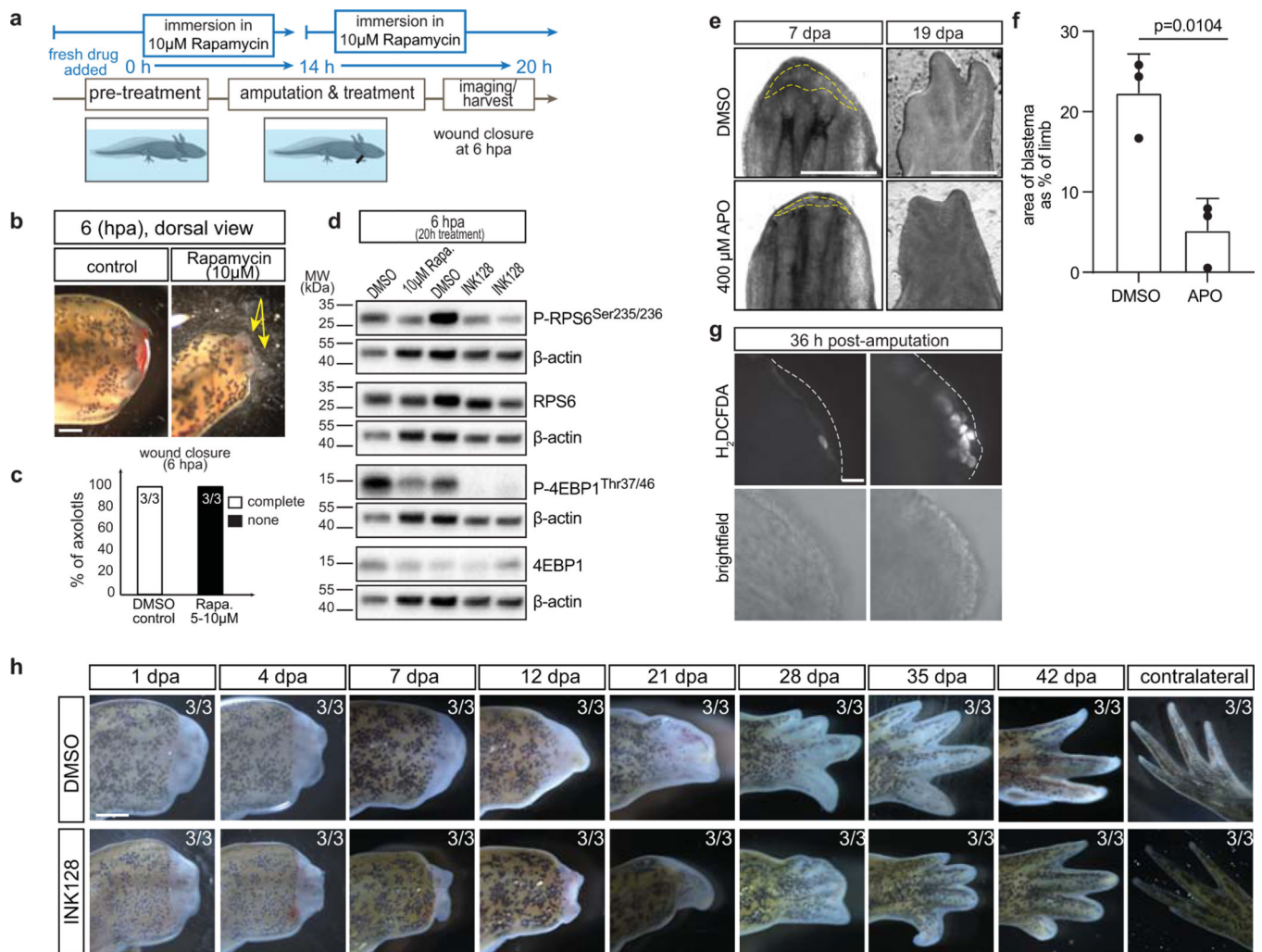

Extended Data Figure 6: Apocynin and INK128 treatments inhibit regeneration

a, Axolotls were pre-treated by immersion in tank water containing 10 μM Rapamycin for 14 h ("pre-treatment", n=3). Limbs were amputated at the forelimb and animals were placed in fresh tank water with a high concentration of Rapamycin (5–10 μM, n=3) for 6 h. **b**, Imaging reveals poor wound closure in animals treated with high concentrations of Rapamycin at 6 hpa. **c**, Tissue harvested from plane of amputation exhibits reduced mTORC1 activation at 6 hpa (n=3 with Rapamycin at 5–10 μM and n=3 DMSO carrier). Yellow arrows point to exposed bone. **d**, Quantitation of phenotypes observed – 3/3 axolotls treated with high concentration of Rapamycin failed to close the wound at 6 hpa. **e**, Representative images of DMSO and Apocynin (APO) treated axolotls reveal reduced blastema size (dashed line) and delayed regeneration in drug-treated animals. **f**, Reduction of blastema size relative to the limb area is shown. An n of 3 animals was used for each condition. Significance was assessed with Student's t-test two-tailed, and a p value < 0.05 was deemed significant. **g**, Additional representative images of control limbs at 36 hpa show presence of dim and bright ROS$^+$ cells stained with H_2DCFDA reported in Fig. 4h-i in which 789 cells analyzed from n=4 DMSO-treated axolotls; 946 cells analyzed from n=5 INK128-treated axolotls. **h**, Representative images of limb regeneration in axolotls treated with DMSO or INK128 4h before amputation performed on n=3 independent axolotls. The INK128-treated animals tracked in this analysis all belong to the 37.5% of animals with partial wound closure at 24 h post-amputation referred to in Figure 4a-b. Mean ± s.d. shown in all plots. Scale bars are 200 px (~1.65 mm) in 6**b**, **g**; 1000 μm in 6**e**; 50 μm in 6**h**.
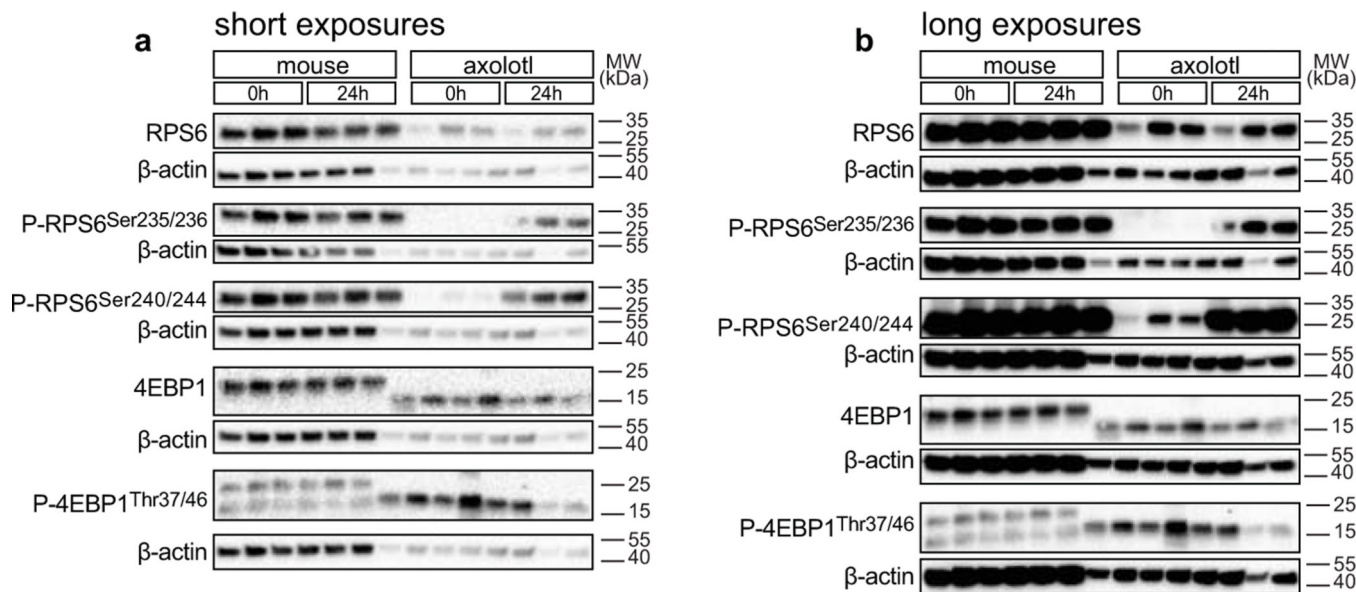
**Extended Data Figure 7: Protein expression in axolotls and mice**

a, Short (~1ms) and **b**, long exposures are provided for the blots shown in Figure 5a to illustrate that differences in mTOR responsiveness to amputation are specific to axolotls independent of exposure time.
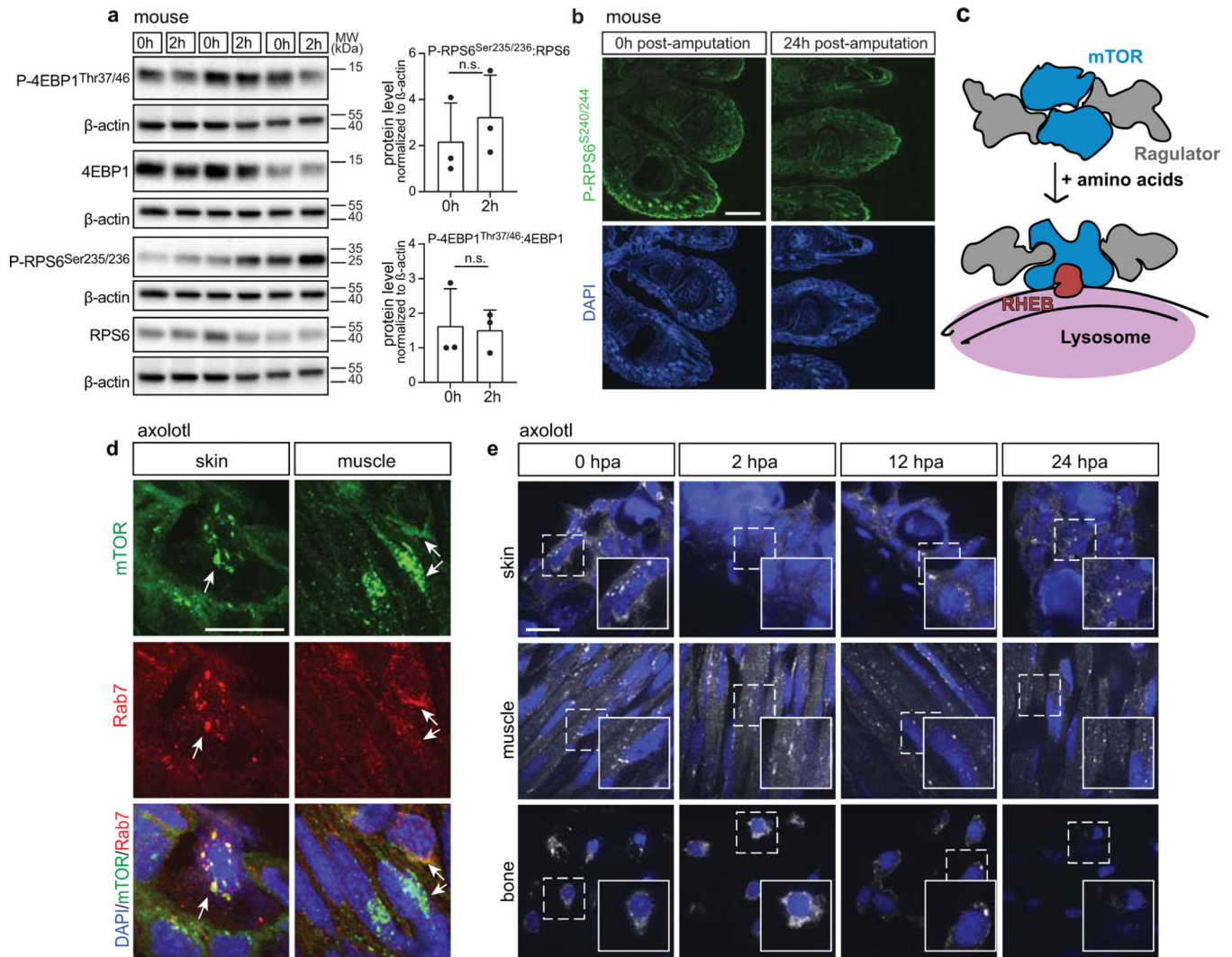
**Extended Data Figure 8: Altered mTOR activity in axolotls and mice**

a, Western blot depicts mTOR activity measured as phosphorylation of P-4EBP1$^{Thr37/46}$ and P-RPS6$^{Ser235/236}$ at 0 h in n=3 individual mice and 2 h post-amputation in n=3 individual mice. Each lane represents a distinct pool of digit tips harvested at given time-point. Quantitation shows ratio of phosphorylated to total protein normalized to ß-actin. P-4EBP1$^{Thr37/46}$ and RPS6 were sequentially blotted on the same membrane and share ß-actin blot. 4EBP1 and P-RPS6$^{Ser235/236}$ were sequentially blotted on another membrane and share ß-actin. **b**, Immunofluorescent staining of mouse digits at 0 and 24 hpa reveals no changes in P-RPS6$^{Ser240/244}$ expression after proximal amputation performed on tissues from n=3 individual mice. **c**, Schematic depicts amino acid dependent translocation of mTORC1 to the lysosome is required for pathway activation. **d**, Rab7 (red), mTOR (green) and nuclear stain (DAPI/blue) in axolotl tissues at 24 h post-amputation illustrate co-localization of mTOR to lysosomes, n=2 individual axolotls. **e**, Immunofluorescence staining of axolotl tissues depicts punctate mTOR localization (white/grey) and nuclei (DAPI/blue) in cells of the skin, muscle and bone near the wound site at 0, 2, 12, and 24 h post-amputation (hpa). Tissues from n=1 axolotl per time-point. Mean ± s.d. are shown

in all plots. Scale bar is 500 μm in 8**b**; 25 μm in 8**d, e**. Student's t-test, two-tailed, was used to assess significance in a, and p > 0.05 deemed not significant (n.s.).
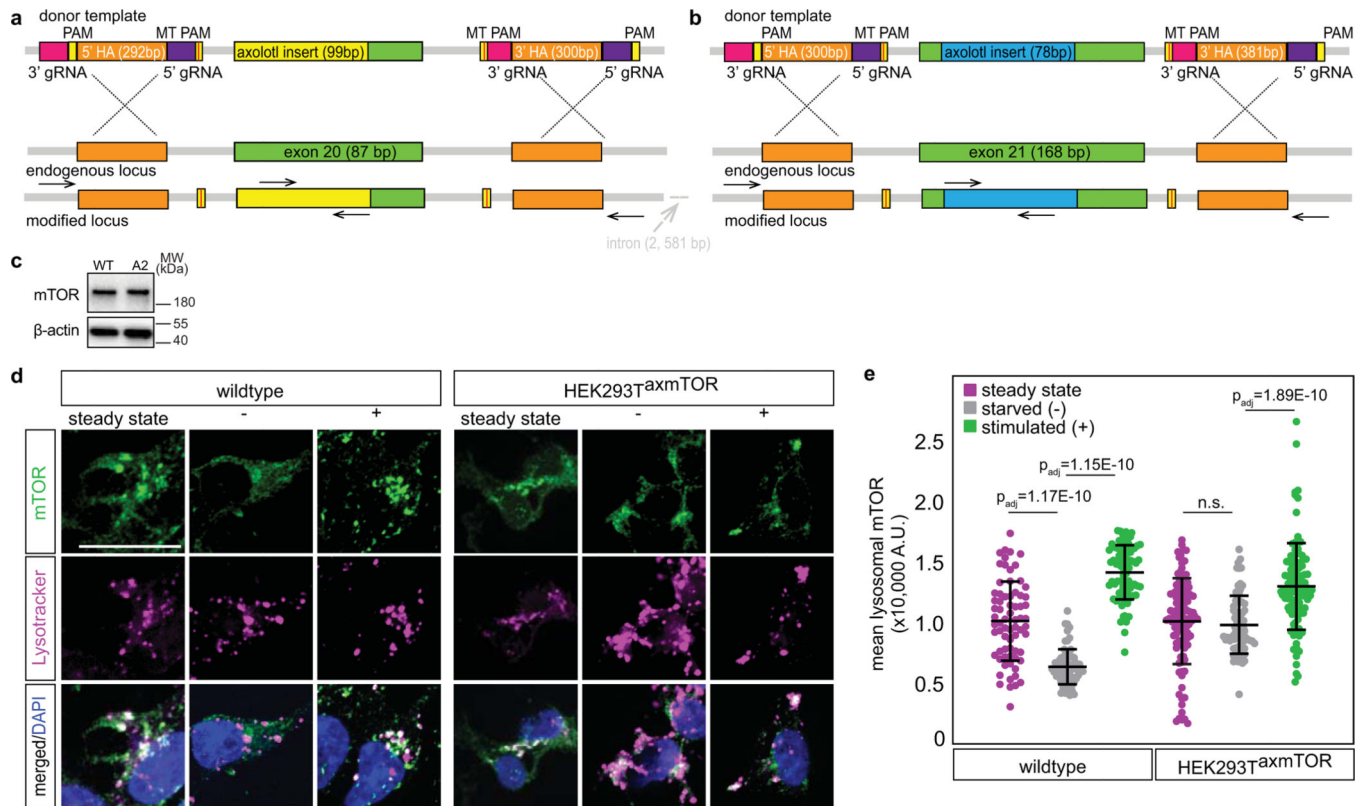
Extended Data Figure 9: Axolotl insertions promote lysosomal retention of mTOR
a, Schematic depicts/Cas9 targeting strategy to introduce axolotl insert 1 in-frame into exon 20 of human mTOR in HEK 293T cells. gRNA (guide RNA site), HA (homology arm), PAM (protospacer adjacent motif) MT PAM (mutated protospacer motif). **b**, Schematic depicts CRISPR/Cas9 strategy to introduce axolotl insert 2 in-frame into exon 21 of human mTOR in HEK 293T cells. **c**, Western blot analysis illustrates steady-state expression of mTOR protein at steady state in wildtype HEK 293T cells and HEK 239T[axmTOR], n=3 independent experiments. **d**, Immunofluorescence staining of mTOR (green), lysosomes (Lysotracker in magenta) and nuclei (DAPI) in wildtype and HEK 239T[axmTOR] cells at steady state, upon starvation (−), and stimulation. Scale bar is 25 μm. **e**, Quantitation of mean mTOR intensity within lysosomes. For each cell line and condition, the lysosomal intensity is expressed relative to the mean steady state intensity for that specific cell line. Two independently derived cell lines were examined for each genotype. The following cell numbers were pooled by treatment or genotype after three independent experiments (WT at steady state from parental WT line or A3 wildtype clone (70 cells), starved (71 cells), fed (81 cells) and HEK 239T[axmTOR] cells from C1 or A2 double mutant clones at steady state (103 cells), starved (75 cells), fed (102) cells. Significance assessed with one-way ANOVA (p<1.0E-15). Exact adjusted p-values (Tukey's multiple comparison test, 95% CI) for individual multiple comparisons are shown in the figure. Mean ± s.d. are shown in all plots.
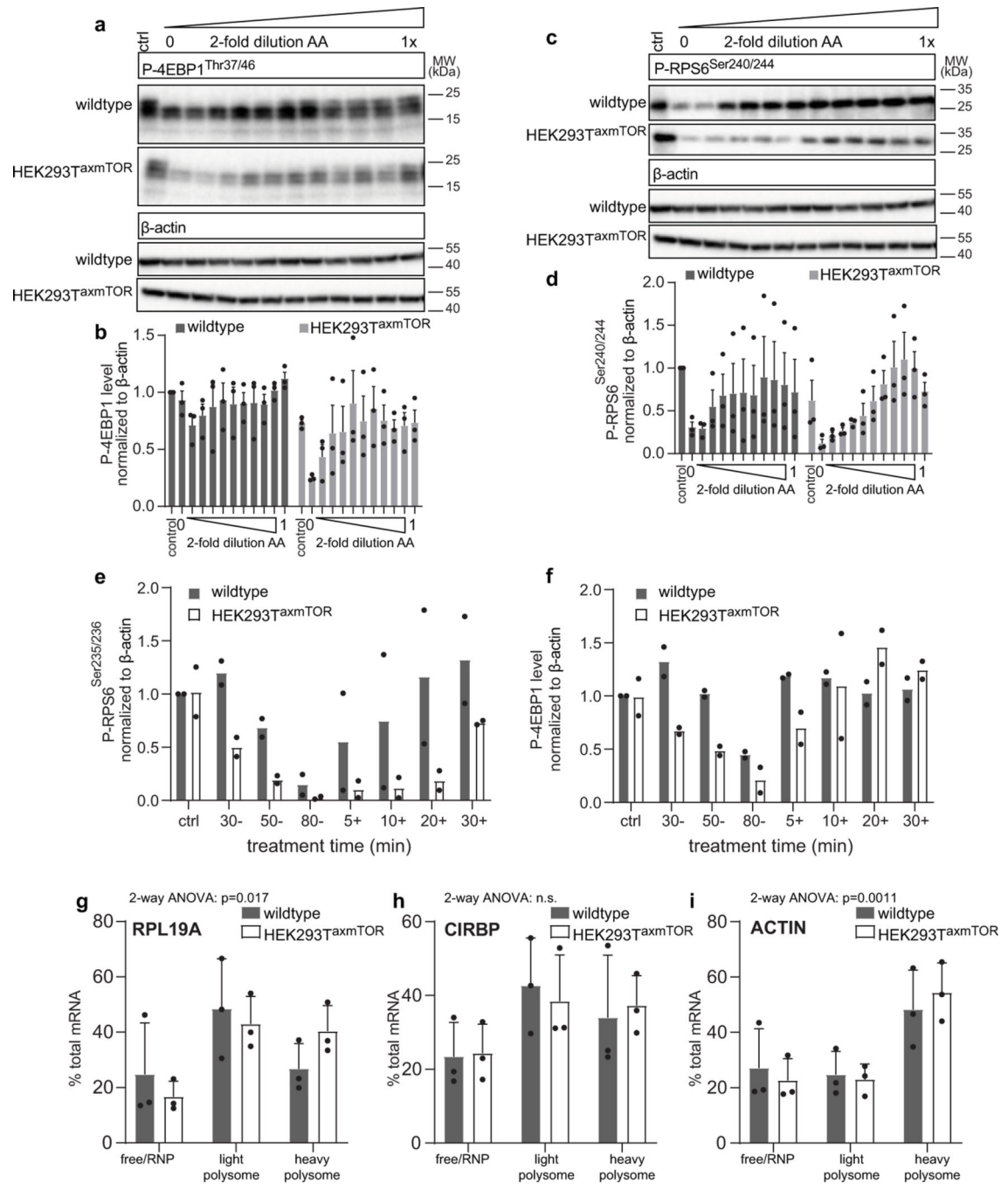
Extended Data Figure 10: Axolotl insertions promote increased nutrient sensitivity
a, Representative western blot (n=3) of amino acid (AA) titration experiment illustrates greater sensitivity of P-4EBP1$^{Thr37/46}$ phosphorylation in HEK 293T^{axmTOR} to amino acid concentration. **b**, Quantitation P-4EBP1$^{Thr37/46}$ level normalized to ß-actin. **c**, Representative western blot (n=3) of AA titration illustrates greater sensitivity of P-RPS6$^{Ser240/244}$ phosphorylation in response to change to AA levels. **e**, Quantitation of P-RPS6$^{Ser235/236}$ level and **f**, P-4EBP1$^{Thr37/46}$ level each normalized to ß-actin in wildtype and HEK 239T^{axmTOR} and HEK 239T^{axmTOR} cells in 2 independent experiments and

normalized to the control (target protein level in wildtype HEK293T cells at steady state). Data illustrates that axolotl mTOR is better at sensing nutrient withdrawal over time. **g,** Graphs depict the level of a given mRNA detected by qPCR in pooled free/RNP, light or heavy polysome fractions 6 hours after re-feeding of starved wildtype or HEK293T[axmTOR] cells. A significant shift from the free-fraction to the heavy polysome is observed for RPL19. **h,** no change is observed for CIRBP (n.s.), **i,** a significant shift is observed for ß-actin. For **g-i,** the experiment was performed three times and data represent n=3 independent replicates. Significance was assessed with two-way ANOVA and exact p-values are indicated on the graphs. A p-value < 0.05 was deemed significant. Mean ± s.d. are shown in all plots.

Supplementary Material

Refer to Web version on PubMed Central for supplementary material.

Acknowledgements

Data availability

Source data are provided with this paper. Raw sequencing data supporting this work is available at Gene Expression Omnibus (GSE185593), all other numerical data is in the accompanying Source Data files, all raw western blot data is included in a fully annotated file in Supplementary Data 1.

References

1. McCusker C, Bryant SV & Gardiner DM The axolotl limb blastema: cellular and molecular mechanisms driving blastema formation and limb regeneration in tetrapods. Regeneration 2, 54–71 (2015). [PubMed: 27499868]

2. Monaghan JR et al. Microarray and cDNA sequence analysis of transcription during nerve-dependent limb regeneration. BMC Biol. 7, 1 (2009). [PubMed: 19144100]

3. Stewart R et al. Comparative RNA-seq analysis in the unsequenced axolotl: the oncogene burst highlights early gene expression in the blastema. PLoS Comput. Biol. 9, (2013).

4. Knapp D et al. Comparative transcriptional profiling of the axolotl limb identifies a tripartite regeneration-specific gene program. PLoS One 8, e61352 (2013). [PubMed: 23658691]

5. Bryant DM et al. A tissue-mapped axolotl de novo transcriptome enables identification of limb regeneration factors. Cell Rep. 18, 762–776 (2017). [PubMed: 28099853]

6. Nowoshilow S et al. The axolotl genome and the evolution of key tissue formation regulators. Nature 554, 50–55 (2018). [PubMed: 29364872]

7. Johnson K, Bateman J, DiTommaso T, Wong AY & Whited JL Systemic cell cycle activation is induced following complex tissue injury in axolotl. Dev. Biol. 433, 461–472 (2018). [PubMed: 29111100]

8. Storer MA et al. Acquisition of a Unique Mesenchymal Precursor-like Blastema State Underlies Successful Adult Mammalian Digit Tip Regeneration. Dev. Cell 52, 509–524 (2020). [PubMed: 31902657]

9. Gerber T et al. Single-cell analysis uncovers convergence of cell identities during axolotl limb regeneration. Science 362, eaaq0681 (2018).

10. Leigh ND et al. Transcriptomic landscape of the blastema niche in regenerating adult axolotl limbs at single-cell resolution. Nat. Commun. 9, 5153 (2018). [PubMed: 30514844]

11. Hanschmann E-M, Godoy JR, Berndt C, Hudemann C & Lillig CH Thioredoxins, glutaredoxins, and peroxiredoxins—molecular mechanisms and health significance: from cofactors to antioxidants to redox signaling. Antioxid. Redox Signal. 19, 1539 (2013). [PubMed: 23397885]

12. Pol A et al. Mutations in SELENBP1, encoding a novel humanmethanethiol oxidase, cause extra-oral halitosis. Nat. Genet. 50, 120 (2018). [PubMed: 29255262]

13. Love NR et al. Amputation-induced reactive oxygen species are required for successful Xenopus tadpole tail regeneration. Nat. Cell Biol. 15, 222–228 (2013). [PubMed: 23314862]

14. Pirotte N et al. Reactive oxygen species in planarian regeneration: an upstream necessity for correct patterning and brain formation. Oxid. Med. Cell. Longev. 2015, (2015).

15. Baddar NWAH, Chithrala A & Voss SR Amputation-induced ROS signaling is required for axolotl tail regeneration. Dev. Dyn. 248, 189 (2019). [PubMed: 30569660]

16. Carbonell BM, Cardona JZ & Delgado JP Hydrogen peroxide is necessary during tail regeneration in juvenile axolotl. Dev. Dyn. 251, 1076 (2022).

17. Oshi M et al. Annexin A1 Expression Is Associated with Epithelial-Mesenchymal Transition (EMT), Cell Proliferation, Prognosis, and Drug Response in Pancreatic Cancer. Cells 10, 653 (2021). [PubMed: 33804148]

18. Kumar A, Godwin JW, Gates PB, Garza-Garcia AA & Brockes JP Molecular basis for the nerve dependence of limb regeneration in an adult vertebrate. Science 318, 772–777 (2007). [PubMed: 17975060]

19. Hsieh AC et al. The translational landscape of mTOR signalling steers cancer initiation and metastasis. Nature 485, 55–61 (2012). [PubMed: 22367541]

20. Thoreen CC et al. A unifying model for mTORC1-mediated regulation of mRNA translation. Nature 485, 109–13 (2012). [PubMed: 22552098]

21. Rodgers JT et al. mTORC1 controls the adaptive transition of quiescent stem cells from G0 to GAlert. Nature 510, 393–396 (2014). [PubMed: 24870234]

22. Hirose K, Shiomi T, Hozumi S & Kikuchi Y Mechanistic target of rapamycin complex 1 signaling regulates cell proliferation, cell survival, and differentiation in regenerating zebrafish fins. BMC Dev. Biol. 14, 42 (2014). [PubMed: 25480380]

23. González-Estévez C et al. SMG-1 and mTORC1 Act Antagonistically to Regulate Response to Injury and Growth in Planarians. PLoS Genet. 8, e1002619 (2012).

24. Liu GY & Sabatini DM mTOR at the nexus of nutrition, growth, ageing and disease. Nature Reviews Molecular Cell Biology 21, 183–203 (2020). [PubMed: 31937935]

25. Holz MK, Ballif BA, Gygi SP & Blenis J mTOR and S6K1 Mediate Assembly of the Translation Preinitiation Complex through Dynamic Protein Interchange and Ordered Phosphorylation Events. Cell 123, 569–580 (2005). [PubMed: 16286006]

26. Gingras AC et al. Hierarchical phosphorylation of the translation inhibitor 4E-BP1. Genes Dev. 15, 2852–2864 (2001). [PubMed: 11691836]

27. Meyuhas O Ribosomal protein S6 phosphorylation: four decades of research. Int. Rev. Cell Mol. Biol. 320, 41–73 (2015). [PubMed: 26614871]

28. Roux PP et al. RAS/ERK signaling promotes site-specific ribosomal protein S6 phosphorylation via RSK and stimulates cap-dependent translation. J. Biol. Chem. 282, 14056–14064 (2007). [PubMed: 17360704]

29. Sonenberg N & Hinnebusch AG Regulation of translation initiation in eukaryotes: mechanisms and biological targets. Cell 136, 731–745 (2009). [PubMed: 19239892]

30. Choo AY, Yoon S-O, Kim SG, Roux PP & Blenis J Rapamycin differentially inhibits S6Ks and 4E-BP1 to mediate cell-type-specific repression of mRNA translation. Proc. Natl. Acad. Sci. U. S. A. 105, 17414–9 (2008). [PubMed: 18955708]

31. Feldman ME et al. Active-Site Inhibitors of mTOR Target Rapamycin-Resistant Outputs of mTORC1 and mTORC2. PLoS Biol. 7, e1000038 (2009). [PubMed: 19209957]

32. Thoreen CC et al. An ATP-competitive mammalian target of rapamycin inhibitor reveals rapamycin-resistant functions of mTORC1. J. Biol. Chem. 284, 8023–8032 (2009). [PubMed: 19150980]

33. Moerke NJ et al. Small-molecule inhibition of the interaction between the translation initiation factors eIF4E and eIF4G. Cell 128, 257–67 (2007). [PubMed: 17254965]

34. Chandra J, Samali A & Orrenius S Triggering and modulation of apoptosis by oxidative stress. Free Radic. Biol. Med. 29, 323–333 (2000). [PubMed: 11035261]

35. Sancak Y et al. Ragulator-Rag complex targets mTORC1 to the lysosomal surface and is necessary for its activation by amino acids. Cell 141, 290–303 (2010). [PubMed: 20381137]

36. Sancak Y et al. The rag GTPases bind raptor and mediate amino acid signaling to mTORC1. Science 320, 1496–1501 (2008). [PubMed: 18497260]

37. Long X, Lin Y, Ortiz-Vega S, Busch S & Avruch J The Rheb switch 2 segment is critical for signaling to target of rapamycin complex 1. J. Biol. Chem. 282, 18542–18551 (2007). [PubMed: 17470430]

38. Takahara T, Hara K, Yonezawa K, Sorimachi H & Maeda T Nutrient-dependent multimerization of the mammalian target of rapamycin through the N-terminal HEAT repeat region. J. Biol. Chem. 281, 28605–28614 (2006). [PubMed: 16870609]

39. Ma C et al. L-leucine promotes axonal outgrowth and regeneration via mTOR activation. FASEB J. 35, e21526 (2021). [PubMed: 33813773]

40. Abrams MJ et al. A conserved strategy for inducing appendage regeneration in moon jellyfish, Drosophila, and mice. Elife 10, (2021).

41. Pereira MG et al. Leucine supplementation improves skeletal muscle regeneration after cryolesion in rats. PLoS One 9, 85283 (2014).

42. Villiard E et al. Urodele p53 tolerates amino acid changes found in p53 variants linked to human cancer. BMC Evol. Biol. 7, 180 (2007). [PubMed: 17903248]

43. Brockes JP Regeneration and cancer. Biochim. Biophys. Acta - Rev. Cancer 1377, (1998).

44. Yang H et al. Mechanisms of mTORC1 activation by RHEB and inhibition by PRAS40. Nature 552, 368–373 (2017). [PubMed: 29236692]

45. Rogala KB et al. Structural basis for the docking of mTORC1 on the lysosomal surface. Science 366, 468–475 (2019). [PubMed: 31601708]

46. Schulte ML et al. Pharmacological Blockade of ASCT2-dependent Glutamine Transport Leads To Anti-tumor Efficacy in Preclinical Models. Nat. Med. 24, 194 (2018). [PubMed: 29334372]

47. Nicklin P et al. Bidirectional transport of amino acids regulates mTOR and autophagy. Cell 136, 521–534 (2009). [PubMed: 19203585]

48. Hirose K et al. Evidence for hormonal control of heart regenerative capacity during endothermy acquisition. Science 364, 184–188 (2019). [PubMed: 30846611]

49. Pause A et al. Insulin-dependent stimulation of protein synthesis by phosphorylation of a regulator of 5'-cap function. Nature 371, 762–767. (1994). [PubMed: 7935836]

50. Baumann K Cell signalling: How mTORC1 senses leucine. Nat. Rev. Mol. Cell Biol. 16, 699 (2015). [PubMed: 26530388]

51. Liu J, Xu Y, Stoleru D & Salic A Imaging protein synthesis in cells and tissues with an alkyne analog of puromycin. Proc. Natl. Acad. Sci. U. S. A. 109, 413–8 (2012). [PubMed: 22160674]

52. Ingolia NT, Brar GA, Rouskin S, McGeachy AM & Weissman JS The ribosome profiling strategy for monitoring translation in vivo by deep sequencing of ribosome-protected mRNA fragments. Nat. Protoc. 7, 1534–50 (2012). [PubMed: 22836135]

53. Smith JJ et al. A chromosome-scale assembly of the axolotl genome. Genome Res. 29, 317–324 (2019). [PubMed: 30679309]

54. Floor SN & Doudna JA Tunable protein synthesis by transcript isoforms in human cells. Elife 5, 1–25 (2016).

55. Bolger AM, Lohse M & Usadel B Trimmomatic: a flexible trimmer for Illumina sequence data. Bioinformatics 30, 2114–2120 (2014). [PubMed: 24695404]

56. Li B & Dewey CN RSEM: accurate transcript quantification from RNA-Seq data with or without a reference genome. BMC Bioinforma. 2011 121 12, 1–16 (2011).

57. Langmead B & Salzberg SL Fast gapped-read alignment with Bowtie 2. Nat. Methods 2012 94 9, 357–359 (2012).

58. Robinson MD, McCarthy DJ & Smyth GK edgeR: a Bioconductor package for differential expression analysis of digital gene expression data. Bioinformatics 26, 139–40 (2010). [PubMed: 19910308]

59. Ritchie ME et al. limma powers differential expression analyses for RNA-sequencing and microarray studies. Nucleic Acids Res. 43, e47–e47 (2015). [PubMed: 25605792]

60. Law CW, Chen Y, Shi W & Smyth GK voom: precision weights unlock linear model analysis tools for RNA-seq read counts. Genome Biol. 2014 152 15, 1–17 (2014).

61. Dennis G et al. DAVID: database for annotation, visualization, and integrated discovery. Genome Biol. 2003 49 4, 1–11 (2003).

62. Benjamini Y & Hochberg Y Controlling the false discovery rate: a practical and powerful approach to multiple testing. J. R. Stat. Soc. Ser. B 57, 289–300 (1995).

63. Yang J et al. Improved protein structure prediction using predicted interresidue orientations. Proc. Natl. Acad. Sci. 117, 1496–1503 (2020). [PubMed: 31896580]

64. Sancak Y et al. Ragulator-rag complex targets mTORC1 to the lysosomal surface and is necessary for its activation by amino acids. Cell 141, 290–303 (2010). [PubMed: 20381137]

65. Zhang J-P et al. Efficient precise knockin with a double cut HDR donor after CRISPR/Cas9-mediated double-stranded DNA cleavage. Genome Biol. 2017 181 18, 1–18 (2017).

66. Ran F et al. Genome engineering using the CRISPR-Cas9 system. Nat. Protoc. 8, 2281–2308 (2013). [PubMed: 24157548]

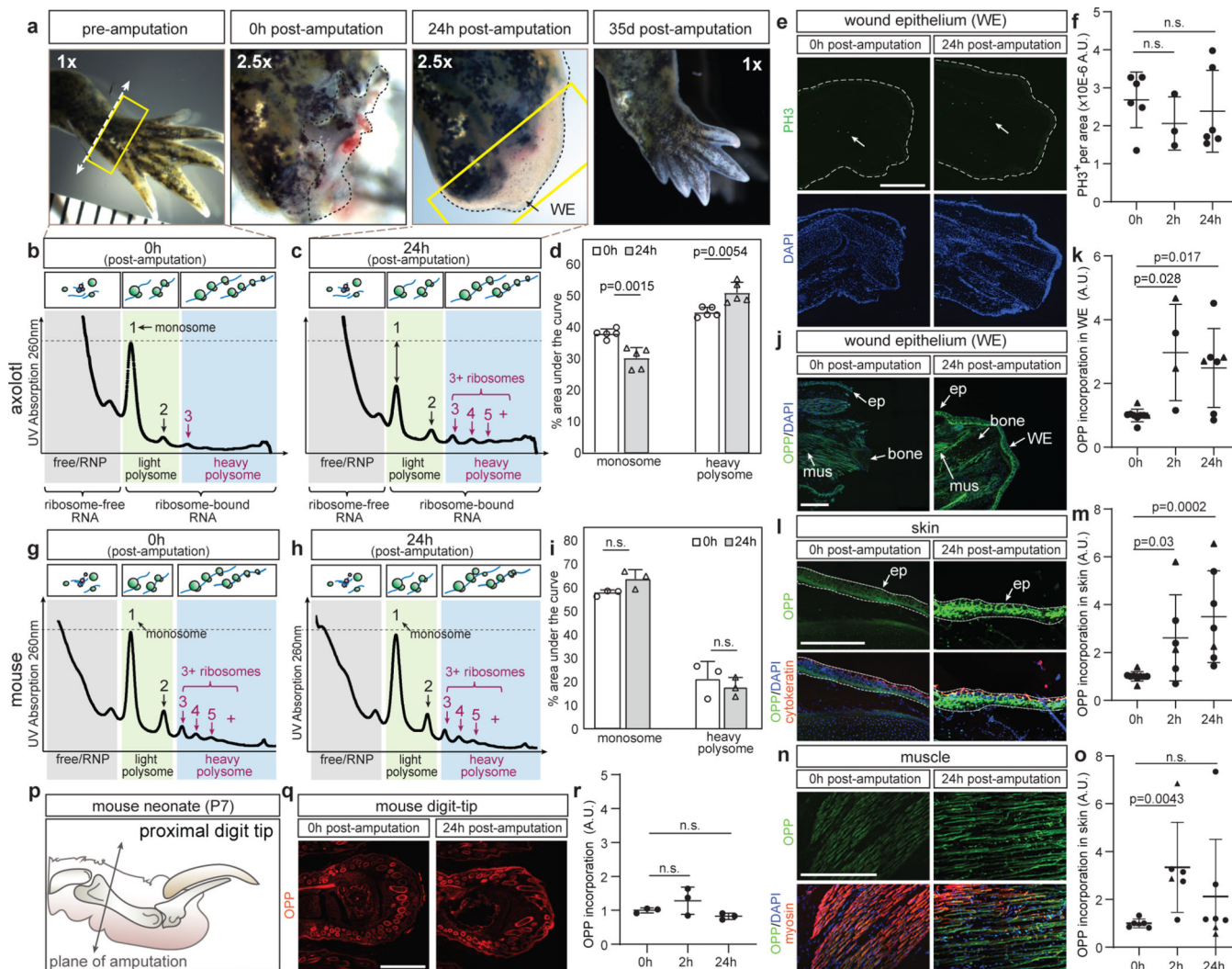**Figure 1: Protein synthesis activation upon injury in axolotls but not in mice.**

a, Axolotl forelimb regeneration (n=3). Amputation plane (dashes) and harvested tissue (box). **b**, Sucrose gradient fractionation at 0 hpa, monosome (dashes), polysome peaks (numbered) at 0 hpa. **c**, Decreased monosome and increased polysome (red arrows) peaks at 24 hpa. **d**, Gradient quantitation at 0 and 24 hpa (n=5). **e**, PH3+ cells in axolotls quantified in **f**, at 0 (n=6), 2 (n=3) and 24 (n=6) hpa. **g**, Sucrose gradient of mouse digits at 0 hpa and **h**, 24 hpa **i**, quantified for n=3 independent pools of digit tissues per time point. **j**, Global OPP increase. **k**, OPP in ep at 0 hpa (n=9) compared to WE at 2 hpa (n=4) or 24 hpa (n=7). **l**, OPP in ep (dashes). **m**, OPP in ep 2 hpa (n=6) or 24 hpa (n=8) compared to 0 hpa (n=9). **n**, OPP in axolotl muscle near wound: OPP (green), heavy chain myosin (red), nuclei (blue) is quantified in **o**, at 0 hpa (n=6) compared to 2 hpa (n=6) or 24 hpa (n=7). **p**, Non-regenerative mouse digit amputation (dashes). **q**, OPP (red) in mouse digits is quantified in **r**, for n=3 animals per time point. In **f**, **k**, **m**, **o**, **r** statistical significance is assessed with Mann-Whitney and with Student's t-test, two-tailed, in **d** and **I**. In **k**, **m** and **o** injections were 20μM (triangles) or 10μM (circles) OPP. All n are independent biological replicates: in **a**, **e-f**, **k**, **m**, **o**, **r** each n is an individual animal, in **b-d** and **g-i** each

n is an independent pool of tissues from 3–5 individual animals. Wound epithelium (WE), epithelium (ep), muscle (mus). All plots show mean ± s.d. Scale bar is 1000 μm in 1**e**, **j** and 500 μm in 1 **l**, **n**, **q**.
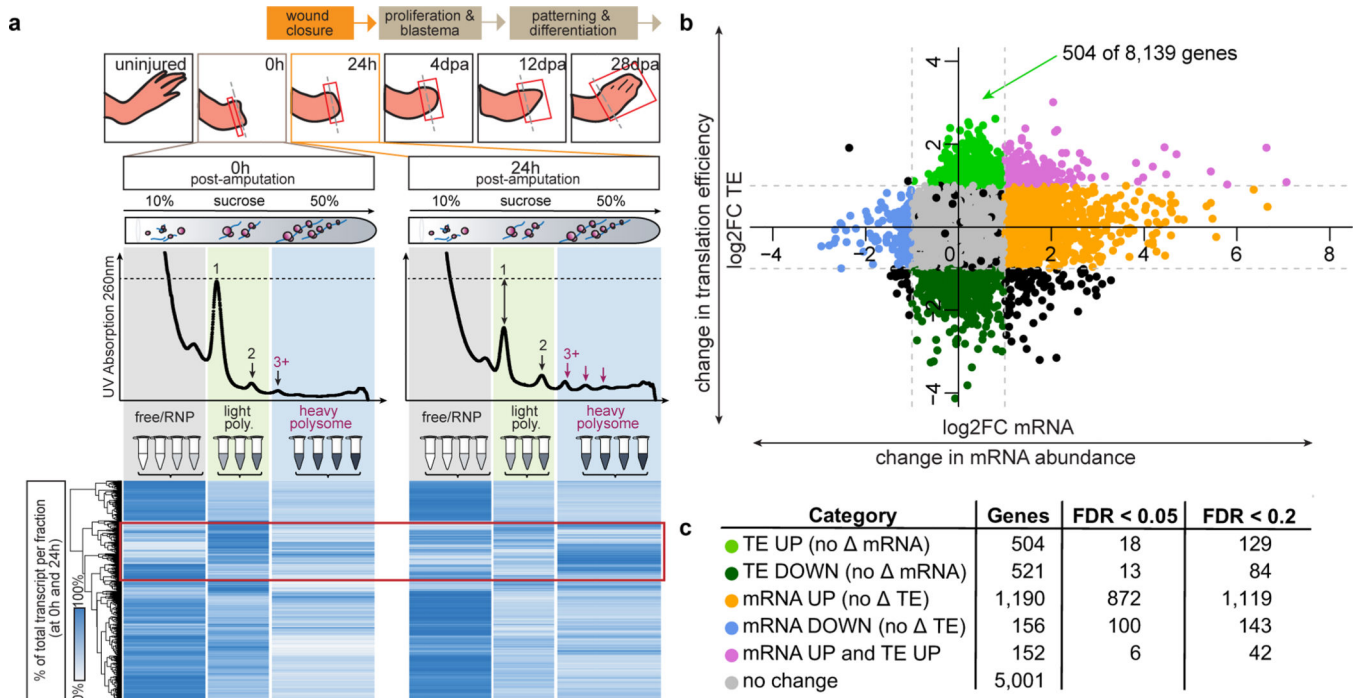
Figure 2: Regenerative translation targets the dormant transcriptome for rapid translational remodeling

a, Polysome sequencing pipeline for tissues at 0 hpa and 24 hpa subjected to sucrose gradient fractionation and RNA-Seq (n=2 biological replicates per time-point for each set of "input" (total lysate), "RNP/free", "light" and "heavy" libraries). Heat map shows percentage of reads of a given mRNA in each fraction. Red box highlights transcript shifts in response to amputation. **b**, Scatter plot depicts (log_2) fold-change (FC) in total mRNA abundance between 0 and 24 hpa on x-axis and (log_2) FC in translation efficiency (TE) on y-axis. Grey dashed lines indicate two-fold change on the log_2 scale. **c**, Color code for transcripts in each category in (**b**) that show a 2-fold change in transcription or TE at false discovery (FDR) cut-offs 0.05 and 0.2.
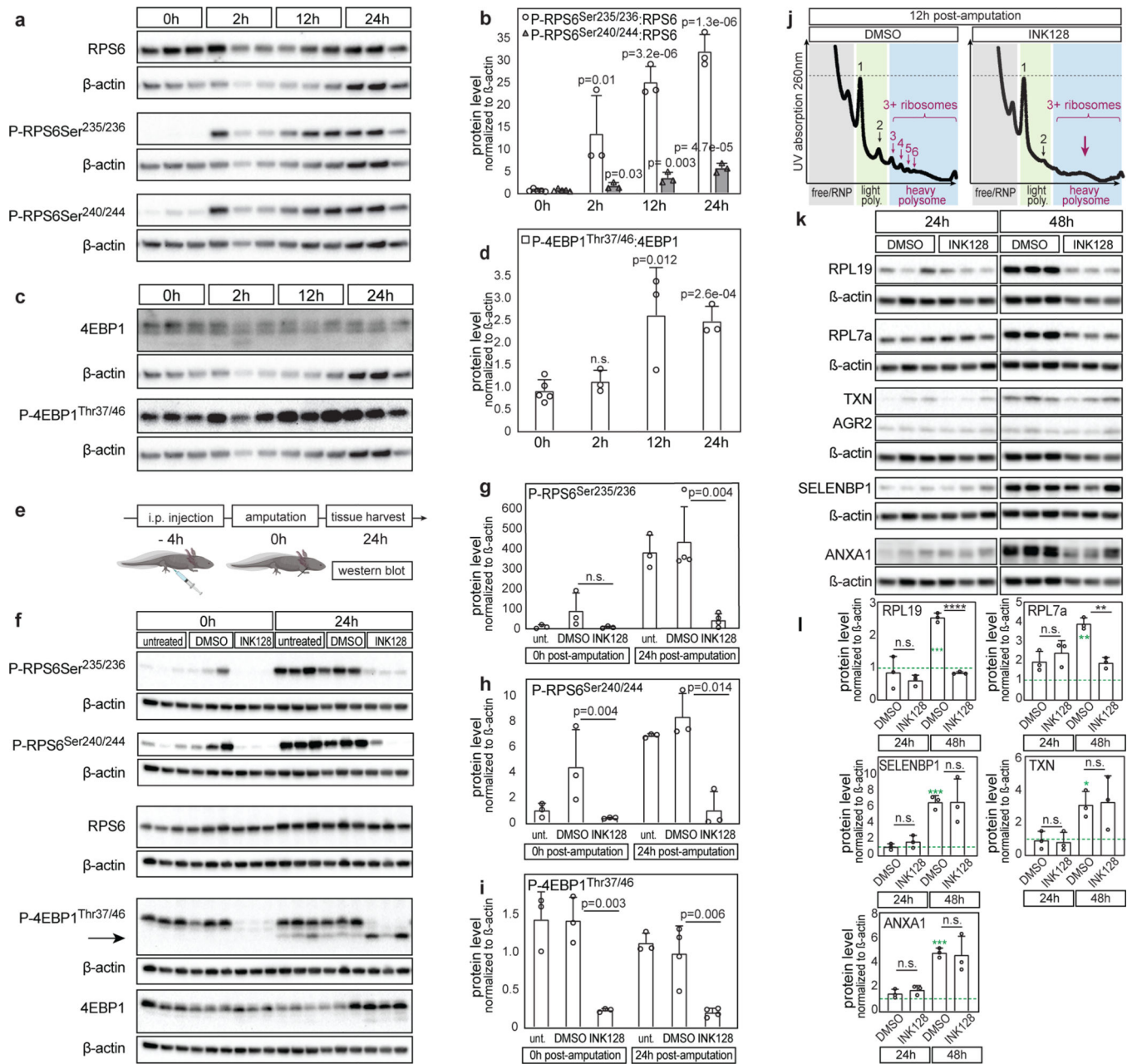
Figure 3: Injury is associated with rapid activation of mTOR signaling in the axolotl
a, P-RPS6 is compared **b**, between 0 hpa and 2, 12 or 24 hpa for P-RPS6$^{Ser235/236}$ and between 0 hpa and 2, 12 or 24 hpa for P- RPS6$^{Ser240/244}$. **c**, P-4EBP1$^{Thr37/46}$ is quantified in **d**, between 0 hpa and 2, 12 or 24 hpa. **e**, Schematic of injection and amputation. **f**, For DMSO vs. INK128 treatment comparison, P-RPS6$^{Ser235/236}$ levels are quantified in **g**, at 0 hpa or 24 hpa. **h**, P-RPS6$^{Ser240/244}$ is quantified at 0 hpa or 24 hpa. **i**, P-4EBP1$^{Thr37/46}$ is quantified at 0 hpa or 24 hpa. Arrow points to P-4EBP2 band. "unt." refers to non-injected animals. For **b-i** exact p-values are shown above bars. **j**, Sucrose gradient shows high translation (numbered arrows) in DMSO-treated and low translation (large arrow) in INK128-treated animals at 12 hpa (n=3 independent tissue pools/treatment).

k, Translationally regulated proteins are quantified in **l**, green asterisks indicate significant target increase (RPL19: p=0.0007, RPL7a: p=0.001, SELENBP1: p=0.003, TXN: p=0.04, ANXA1: p=0.0001) for DMSO controls at 48 vs. 0 hpa (green dash). For DMSO vs. INK128 at 48 hpa, p-values are p=3.44054E-05 (RPL19), p=0.001 (RPL7a). P-values are n.s. for other comparisons. In **a**, **c**, **f** and **k** membranes were sequentially blotted and share ß-actin which is reproduced with accompanying targets for clarity (see Supplementary Data 1 for raw gels). N=3 animals were examined for each condition (except DMSO and INK128 at 24 hpa shown in **g**, **i** where n=4 each). All plots show mean +/− s.d., significance assessed with Student's t-test, two-tailed, where * is p < 0.05, ** is p < 0.01, *** is p < 0.001, **** is p < 0.0001 and n.s. is p > 0.05 and not significant. All bands are normalized to their own ß-actin.
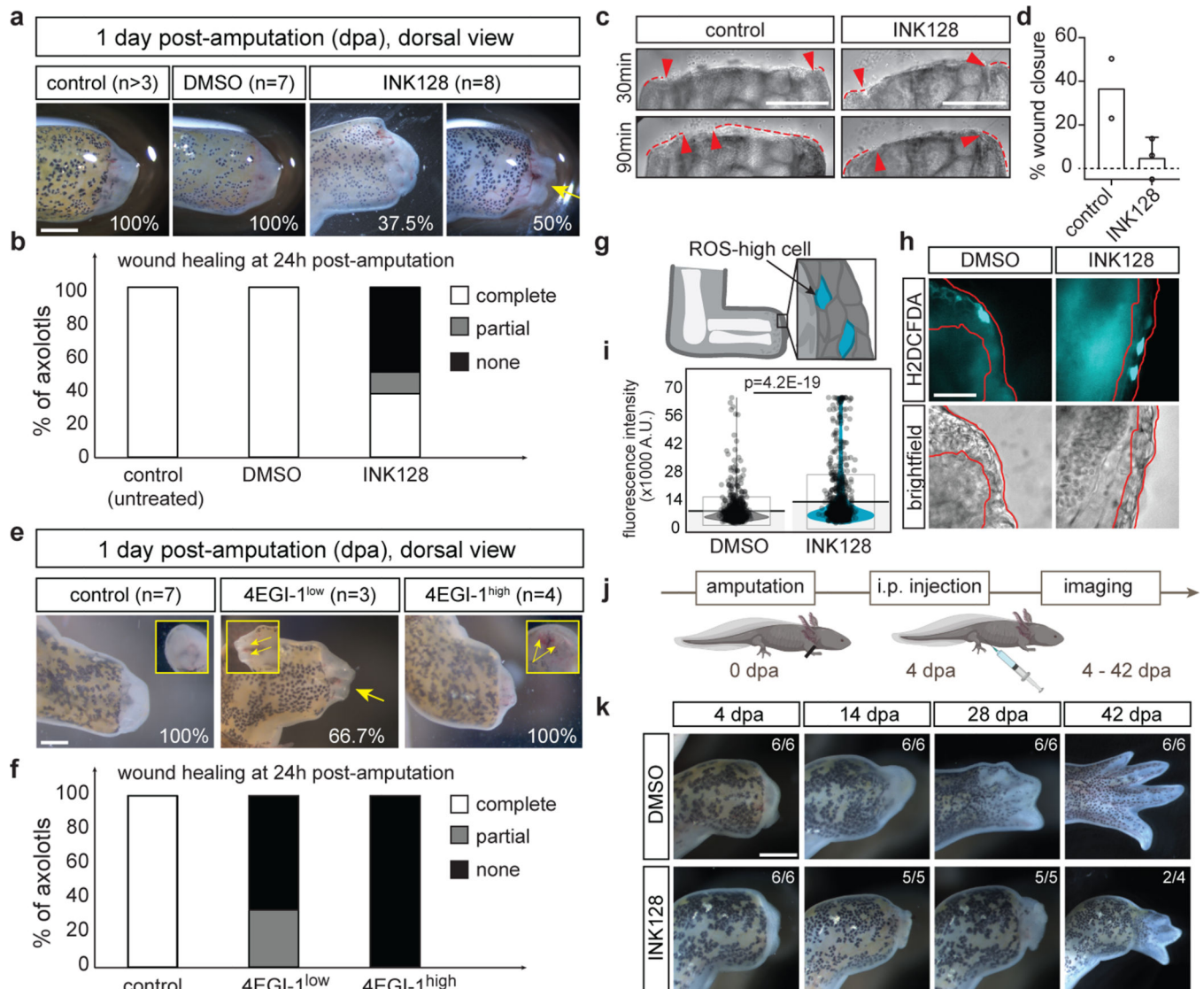
Figure 4: mTOR activation promotes rapid wound closure and regeneration
a, Wound site in untreated (n=3), DMSO (n=7) and INK128 (n=8) treated animals at 1 dpa. **b**, Phenotypes are quantified and indicate "complete" multi-layered wound closure, "partial" closure with a single cell layer at apex or failure of wound closure ("none") with protruding bone. **c**, Cell migration at 30 min and 90 min post-amputation in control (n=2, Supplementary Video 1) and INK128-treated (n=3, Supplementary Video 2) animals. Skin adjacent to wound site (red dashes) and direction of migration (red arrows) shown. **d**, Percentage of wound closed at 1 hpa. Mean ± s.d. **e**, Representative limbs from axolotls treated with low (n=3) or high (n=4) concentration of 4EGI-1 or DMSO (n=7) controls at 24 hpa. Insets show apex of limb with protruding bone (arrow). **f**, Quantitation of wound closure upon 4EGI-1 treatment. **g**, Illustration of ROS high (blue) and low (grey) cells at wound site. **h**, ROS levels in cells, labeled with H_2DCFDA (blue), at the wound site at 36 hpa. **i**, Quantitation of H_2DCFDA fluorescence intensity in the epithelial layer (red) for 789 cells from n=4 DMSO-treated or 946 cells from n=6 INK128-treated axolotls. The plot

min., max., and center values are 2670, 65475, and 6892 for DMSO and 2884, 65535 and 8234 for INK128-treated animals. Black line and box indicate mean +/− s.d., significance assessed with Student's t-test, two-tailed. **j**, Axolotls (n=12) with complete wound closure at 4 dpa treated with DMSO (n=6) or INK128 (n=6) at 4, 6, 8 and 10 dpa. **k**, Images show reduced regeneration in INK128-treated animals imaged at indicated time-points. Fractions (i.e. "6/6") indicate proportion of animals with given phenotype. Scale bars are 200 px (~1.65 mm) in 4**a**, **e**, **k**; 700 μm in 4**c**; 100 μm in 4**h**. Above, n are individual animals.
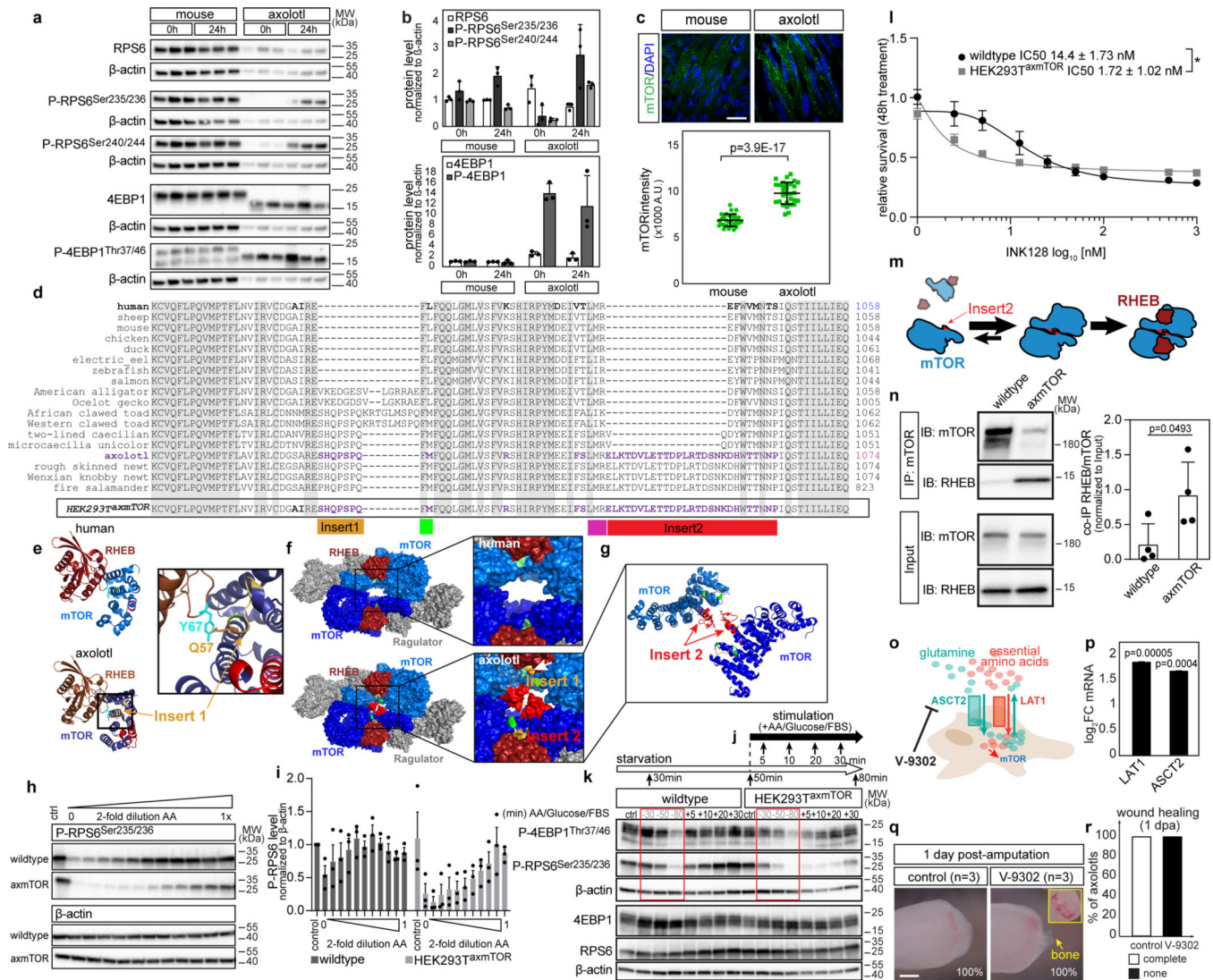
Figure 5: Urodele-specific insertions give rise to hypersensitive mTOR kinase.
a, High basal mTOR activity does not change between 0 and 24 hpa in mouse (n=3 animals/time-point), contrasted to axolotl (n=3 animals/time-point). **b**, Quantitation of phosphorylation. **c**, Intensity of mTOR puncta in muscle at steady state (n=3 animals/ species). Scale bar is 25 μm. **d**, Insert1 (yellow) and insert2 (red) in a multiple sequence alignment. Conserved residues (green, magenta), sequence of HEK 293T^{axmTOR} cells (box). **e**, Structures of human (6BCU) and axolotl RHEB-bound mTOR near the switchII region. Insert1, Q57 (yellow) and RHEB, Y67 (aqua). New interaction interface (inset). **f**, Surface structure shows insert2 (red) filling cavity of mTOR dimer (blue). RHEB (burgundy), Ragulator (grey). **g**, Cartoon view of insert2 dimer. **h**, RPS6 phosphorylation is sensitive to amino acid levels in HEK 293T^{axmTOR}. **i**, Quantitation of P-RPS6$^{Ser235/236}$ (n=3). **j**, Schematic of starvation and re-feeding shown in **k**, for n=2 cell lines per genotype, "ctrl" is steady state. Starvation decreases P-4EBP1$^{Thr37/46}$ and P-RPS6$^{Ser235/236}$ in HEK 293T^{axmTOR}. **l**, Survival assay (n=3 independent replicates) illustrates that insertions confer hypersensitivity on human mTOR kinase. **m**, Insert2 (red) shifts equilibrium in favor of

mTOR dimerization. **n**, Increased binding of RHEB to mTOR in HEK 293T^{axmTOR} cells at steady state (n=4). **o**, V-9302 inhibits ASCT2. **p**, $\log_2$FC in mRNA abundance (0 vs. 24 hpa) in LAT1 and ASCT2. Adjusted p-value shown determined with Benjamini and Hochberg method. **q**, Axolotl limbs at 24 hpa (n=3 each for V-9302 and control). Inset shows protruding bone (arrows) after V-9302 treatment. Scale bar is 200 px (~1.65 mm). % of axolotls with given phenotype quantified in **r**. Mean +/− s.d. shown for **b, c, l, n, p**; mean +/− s.e.m. shown for **i**. In **c, l, n** significance assessed with Student's t-test, two-tailed, exact p-values shown.